Cognitive Robotics 6 (2026) 106–141

Contents lists available at ScienceDirect

Cognitive Robotics

journal homepage: http://www.keaipublishing.com/en/journals/cognitive-robotics/

Research paper

An improved brain emotional learning-based intelligent controller-PID control with adaptive learning rates for MIMO systems

Shahrizal Saat[a,c], Mohd Ashraf Ahmad[b,d,*], Mohd Riduwan Ghazali[b], Mohd Helmi Suid[b]

[a] Faculty of Electronics and Computer Technology and Engineering, Universiti Teknikal Malaysia Melaka, Durian Tunggal, Melaka, 76100, Malaysia
[b] Faculty of Electrical and Electronics Engineering Technology, Universiti Malaysia Pahang Al-Sultan Abdullah, Pekan, Pahang, 26600, Malaysia
[c] Center for Telecommunication Research & Innovation, Universiti Teknikal Malaysia Melaka, Durian Tunggal, Melaka, 76100, Malaysia
[d] Center for Advanced Industrial Technology, Universiti Malaysia Pahang Al-Sultan Abdullah, Pekan, Pahang, 26600, Malaysia

A R T I C L E I N F O

Keywords:
Proportional-integral-derivative (PID) controller
Brain emotional learning-based intelligent controller (BELBIC)
Gantry crane system
Twin rotor multi-input multi-output system (TRMS)
Modified safe experimentation dynamics algorithm (MSEDA)

A B S T R A C T

Advanced multi-input multi-output (MIMO) systems pose significant challenges for trajectory tracking and control energy minimization due to inherent nonlinearities and dynamic coupling. While PID controllers remain widely used, their limited adaptability restricts performance in such environments. Bio-inspired approaches, particularly the brain emotional learning-based intelligent controller (BELBIC), offer improved adaptability; however, the fixed learning rate in standard BELBIC limits responsiveness under varying error signal conditions. This study proposes a BELBIC-PID control scheme with a sigmoid-based adaptive learning rate (SbLR-BELBIC-PID), where the learning rates of the BELBIC components are continuously adjusted, with the PID formulation providing sensory input and reward signals. This adaptive mechanism intensifies or attenuates emotional responses according to deviations from the reference signal, enabling faster convergence and improved control accuracy. Controller parameters are optimized using a modified safe experimentation dynamics algorithm (MSEDA) within a data-driven control framework. The proposed method is validated on the twin-rotor MIMO system and the gantry crane system. Results indicate reductions of 5.24 % and 7.82 % in the fitness function relative to the standard BELBIC-PID. Moreover, the proposed controller achieves lower integral square error, reduced control effort, and enhanced transient response, consistently outperforming conventional PID, NEPID, and standard BELBIC-PID controllers. Robustness evaluations under measurement noise further confirm that SbLR-BELBIC-PID attains lower trajectory-tracking error indices, including IAE, ISE, ITAE, and ITSE. These outcomes demonstrate the effectiveness of adaptive emotional learning for advanced nonlinear control applications.

1. Introduction

Nonlinear multi-input multi-output (MIMO) systems are crucial in many advanced industrial processes that require precise and coordinated regulation of multiple inputs and outputs. Control of such systems is challenging due to inherent nonlinearities, complex interactions among variables, and strong cross-coupling effects, where a change in one input may unintentionally influence multiple

Peer review under the responsibility of KeAi Communications Co., Ltd.
* Corresponding author.
E-mail addresses: mashraf@ump.edu.my, mashraf@umpsa.edu.my (M.A. Ahmad).

https://doi.org/10.1016/j.cogr.2026.02.001
Received 24 December 2024; Received in revised form 9 February 2026; Accepted 28 February 2026
Available online 29 March 2026

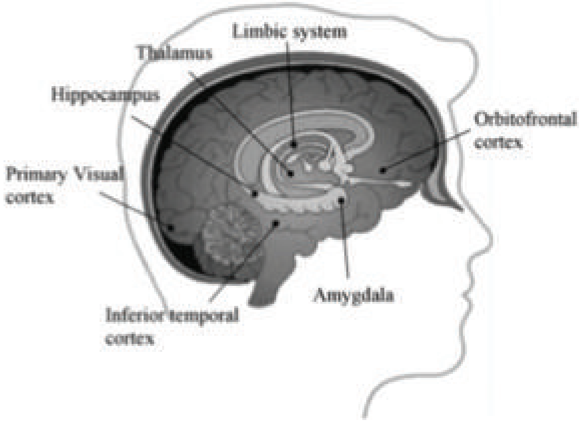

Fig. 1. Structure of emotional learning in the limbic system of the mammalian brain [43].

outputs [1]. These challenges are further exacerbated by dynamic uncertainties and time-varying system parameters, making accurate control difficult to achieve. To address these issues, various advanced control strategies have been proposed, including fuzzy–sliding mode control [2], sliding mode control [3], PID control with input shaping [4], feedback control [5], LQR control [6], and H-infinity control [7]. However, these approaches are predominantly model-based control (MBC) techniques that rely on accurate mathematical representations of the plant. For nonlinear dynamic systems, obtaining precise models is often difficult and prone to errors [8]. Moreover, modeling inaccuracies, unmodeled dynamics, and input–output coupling effects may lead to suboptimal performance, reduced robustness, and potential control instability.

The aforementioned challenges have motivated researchers to explore data-driven control techniques as an alternative to model-based design. Data-driven control reduces reliance on accurate plant models by utilizing measured input–output (I/O) data and treating the plant as a black box [9–11]. Within this framework, optimization algorithms are commonly employed to tune predefined controller structures, where optimal parameters are obtained through iterative procedures until predefined termination criteria are satisfied [12,13]. Among conventional controllers, the proportional–integral–derivative (PID) controller is widely adopted due to its versatility, simple structure, limited tuning parameters, and ease of implementation [12,14–18]. However, despite these advantages, PID controllers exhibit notable limitations in nonlinear MIMO systems, particularly under strong nonlinearities and time-varying dynamics [19]. These limitations are further intensified by complex interactions among multiple inputs and outputs [20], while the inherent linear structure of the PID controller restricts its ability to handle such interdependencies effectively [21]. To overcome these shortcomings, several enhanced PID variants have been proposed, including fractional-order PID (FOPID) controllers [22–24], fuzzy PID controllers [25,26], neural network PID controllers [27–29], and sliding mode PID controllers [30,31].

Although much of the existing research has focused on advanced PID controller variants, bio-inspired controllers offer a promising alternative that warrants further attention. By exploiting principles derived from natural systems, bio-inspired control strategies provide enhanced adaptability and robustness in dynamic environments, enabling performance improvements beyond conventional PID variants. Among these approaches, artificial neural network (ANN) controllers are modeled after the human brain's neural architecture and employ interconnected artificial neurons to generate control actions through weighted connections. Trained using optimization techniques such as backpropagation, ANN controllers can minimize control errors and effectively handle complex nonlinear systems [32]. Their generalization capability further enables adaptation to new system dynamics and external disturbances, making them well suited for real-time control in uncertain and time-varying environments [33]. Another bio-inspired approach is the neuroendocrine-PID (NEPID) controller, which integrates PID control with hormone-like regulatory mechanisms inspired by biological neuroendocrine systems [34,35]. By emulating hormonal feedback loops that regulate homeostasis [36,37], NEPID dynamically adjusts control actions in response to system performance. In addition, immune-based control systems, inspired by biological immune responses, treat disturbances as antigens and generate adaptive reactions based on immune memory, enabling robust control in complex environments [38,39].

Despite the advantages of ANN, NEPID, and immune-based control systems, the brain emotional learning-based intelligent controller (BELBIC) has emerged as one of the most prominent and practically implementable bio-inspired controllers [40]. BELBIC is inspired by emotional learning mechanisms in the mammalian limbic system and enables dynamic adjustment of control actions. Compared with other bio-inspired controllers, it offers rapid adaptation, real-time learning capability, and enhanced robustness derived from emotional learning principles, making it well suited for nonlinear and time-varying MIMO systems. Its model-free structure and reduced computational requirements further support superior control performance in highly nonlinear environments [41]. The BELBIC framework originates from Moren's brain emotional learning (BEL) model introduced in 2001 [42], which describes interactions among the amygdala, orbitofrontal cortex (OFC), and thalamus, as illustrated in Fig. 1 [43]. This model was later extended by Lucas into a closed-loop BELBIC architecture for control engineering applications through the incorporation of external sensory input (SI) and reward signal (RW), enabling adaptation based on real-time feedback signal [40].

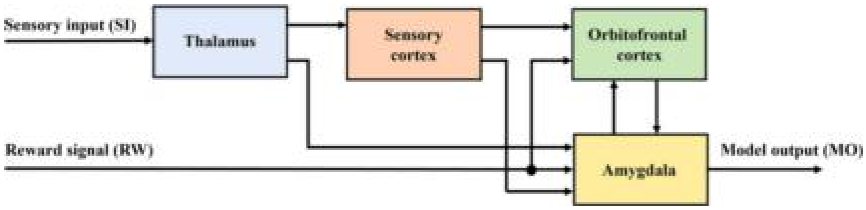

Fig. 2. Schematic of the main configuration of the BELBIC [40].

Designing a BELBIC requires appropriate formulation of the sensory input (SI) and reward signal (RW) functions, which may be defined in terms of the reference signal, controller output, and tracking error signal. These functions govern the emotional learning process and directly influence control performance. In the BELBIC structure, the thalamus performs an initial filtering operation by forwarding dominant sensory information, the amygdala associates sensory input with reinforcement through emotional learning, and the orbitofrontal cortex (OFC) regulates the response by suppressing unsuitable control actions [42]. The general configuration of the BELBIC architecture is shown in Fig. 2 [40]. Once reinforcement learning occurs, BELBIC does not unlearn, which contributes to stability in the learned behavior [44]. This emotional-learning-based feedback mechanism enables adaptive control in dynamically changing environments.

The BELBIC has demonstrated versatility across a wide range of single-input single-output (SISO), single-input multi-output (SIMO), and multi-input multi-output (MIMO) systems. Early studies by Lucas applied BELBIC to control submarine models, robotic arms, gas turbine generators, and switch reluctance motor systems [40]. Subsequent research extended its application to various industrial and robotic systems, including intelligent washing machines [45], micro-heat exchangers [46], magnetic levitation systems [47], unmanned ground vehicles [48], motor drives [49], and inverted pendulum systems [50]. More recent works have reported successful implementation of BELBIC in automotive suspension systems [51], mobile robot motion control [52], islanded microgrids [53], automatic voltage regulators [54], smart structural vibration suppression [55–57], gantry cranes [58], twin-rotor MIMO systems [58], and power converter–driven electric motors [58]. These studies collectively demonstrate the robustness and adaptability of BELBIC, highlighting its potential as a strong alternative to conventional PID-based controllers.

Despite the successful implementation of BELBIC across various systems, further improvement remains possible in its emotional learning process, specifically in terms of learning rate. In the conventional BELBIC controller, the emotional learning rate governs the update of connection weights and is typically set as a constant value [40]. Early studies on brain emotional learning [42] and its implementation in BELBIC [40,58] adopted a fixed learning rate throughout simulations or experiments. While this simplifies controller design, it limits adaptability under varying operating conditions and dynamic changes. A constant learning rate may fail to reflect the varying adaptation requirements of different control scenarios. Rapid disturbances require higher learning rates to reduce tracking errors, whereas steady-state operation benefits from lower learning rates to avoid excessive control action. Consequently, fixed learning-rate mechanisms may restrict the controller's ability to respond effectively to real-time feedback, leading to suboptimal control performance. Moreover, most existing studies have focused on the standard BELBIC with a constant learning rate, and systematic investigation of adaptive emotional learning strategies remains limited.

In control engineering, several adaptive mechanisms have been widely employed to enhance controller performance. Fuzzy-type adaptive controllers adjust parameters using predefined fuzzy rules and provide robustness for nonlinear systems. However, they require extensive rule design and careful tuning, which increases computational complexity [59]. Similarly, actor–critic methods, commonly applied in reinforcement learning–based control, adapt both the control policy and the value function online. This adaptability often yields strong performance but incurs substantial computational demand, particularly for multi-input multi-output systems [60]. Neural-network-based adaptive controllers further offer flexibility by approximating complex nonlinear mappings and enabling real-time adaptation, yet their training and online implementation also involve significant computational effort [61]. Despite their effectiveness, the high complexity of these approaches often limits their practicality for real-time applications. To address these limitations, this study introduces a sigmoid-based adaptive emotional learning rate BELBIC integrated with a PID controller (SbLR-BELBIC-PID), which preserves structural simplicity while enabling dynamic adjustment of the emotional learning process according to variations in the control error signal. The proposed sigmoid function increases the learning rate under large error signals to promote rapid adaptation and decreases it as the error signal diminishes, thereby preventing excessive correction. This mechanism enhances transient responsiveness while maintaining stability during steady-state operation using a computationally efficient technique.

Another challenge in achieving superior control performance lies in determining the optimal control parameters of the SbLR-BELBIC-PID controller. To address this challenge, a data-driven control framework with an online tuning strategy is adopted, where optimization is performed using tracking error signal and control input energy as fitness functions. The modified safe experimentation dynamics algorithm (MSEDA) [58], an enhanced version of the standard safe experimentation dynamics algorithm (SEDA), is employed to identify optimal controller parameters. MSEDA utilizes game-theoretic principles to randomly perturb multiple control parameters during the search process. A linearly decreasing mechanism is used to balance exploration and exploitation, where early iterations emphasize exploration to avoid local optima, while later iterations focus on exploitation to refine control accuracy. In addition, MSEDA preserves the best solution at each update and remains robust to delays or interruptions, since its coefficients are independent of the total number of iterations.

The proposed SbLR-BELBIC-PID controller extends earlier work reported in Ref. [58], where a standard BELBIC-PID controller with a fixed emotional learning rate was implemented. Although that technique demonstrated the feasibility of integrating BELBIC with PID control, its control performance was limited by the learning rate's inability to adapt to changing operating conditions. In this study, the limitation is addressed by replacing the constant learning rate with a sigmoid-based adaptive emotional learning rate, enabling dynamic adjustment in response to variations in the control error signal. The effectiveness of the proposed controller is quantitatively evaluated using fitness functions based on the integral square error (ISE) and integral square input (ISI), together with standard time-domain performance indices, including settling time, rise time, and maximum overshoot. In addition, robustness is assessed through trajectory-tracking case studies under measurement noise.

Based on these considerations, the key contributions presented in this study can be summarized as follows:

(i) This study introduces a sigmoid-based adaptive emotional learning rate integrated into a BELBIC-PID controller, referred to as the SbLR-BELBIC-PID. Unlike the standard BELBIC-PID controller with a fixed learning rate [58], the proposed mechanism dynamically adjusts the emotional learning rate in response to variations in the control error signal, thereby enhancing adaptation capability while preserving a simple and computationally efficient controller structure.

(ii) A data-driven control framework with online parameter tuning is developed to optimize the SbLR-BELBIC-PID controller parameters using the modified safe experimentation dynamics algorithm (MSEDA). The proposed framework enables efficient tuning of high-dimensional controller parameters by balancing exploration and exploitation without requiring an accurate mathematical model of the plant, relying solely on the tracking error signal and control input energy as performance criteria.

(iii) Comprehensive control performance evaluation is conducted using both fitness-function-based indices and standard time-domain performance measures, including integral square error, integral square input, settling time, rise time, and maximum overshoot. The proposed controller is systematically compared with benchmark controllers, including the standard BELBIC-PID [58], NEPID [36], and conventional PID [36], demonstrating improved control accuracy for nonlinear MIMO systems.

(iv) The robustness of the proposed SbLR-BELBIC-PID controller is further validated under measurement noise conditions. Robustness evaluation using integral performance indices, including IAE, ISE, ITAE, and ITSE, confirms that the adaptive emotional learning mechanism enhances control responsiveness and robustness while maintaining stability when compared with the standard BELBIC-PID [58].

This paper is structured as follows. Section 2 presents the problem formulation for the proposed SbLR-BELBIC-PID control of MIMO systems using a data-driven approach to minimize the fitness function. Section 3 details the controller design, followed by Section 4, which describes its tuning via MSEDA. Section 5 evaluates the controller on nonlinear MIMO systems, specifically the TRMS and container gantry crane, with comparisons to BELBIC-PID, NEPID, and PID. Finally, Section 6 concludes the study and highlights the key findings.

Notation: The symbol $\mathbb{R}$ represents the set of real numbers, while $\mathbb{R}_+$ denotes the set of positive real numbers. The notation $\mathbb{R}^n$ indicates a collection of n real numbers. The vectors **0** and **1** consist entirely of zeros and ones, respectively.

2. Problem formulation

Fig. 3 presents a detailed schematic illustration of the computational model of the emotional learning process in the limbic system [42]. The external stimuli to BELBIC, represented by the SI and RW, are derived from the PID controller used in the proposed controller. In the original BELBIC structure [58], the emotional learning rates for the thalamus, amygdala, and orbitofrontal cortex are constant, represented by ε, α and β, respectively, as shown in Fig. 3. In contrast, the proposed SbLR-BELBIC-PID controller uses a sigmoid-based function to dynamically adjust the emotional learning rates for these components within the limbic system. This adaptive mechanism is expected to enhance the quality of emotional learning and improve control accuracy. Further details on the adaptive emotional learning rate mechanism are provided in Section 3.

Fig. 4 presents the MIMO control systems that integrate the SbLR-BELBIC-PID controller. In this framework, the reference input is defined as $\boldsymbol{r}(t) \in \mathbb{R}^q$. The control input is represented by $\boldsymbol{u}(t) \in \mathbb{R}^p$, while the output response is denoted as $\boldsymbol{y}(t) \in \mathbb{R}^q$. The notation G represents the MIMO systems with p inputs and q outputs. Additionally, the sample period is t_s and the discrete time instances are defined as $t = 0,\ t_s,\ 2t_s,\ 3t_s \dots (D-1)t_s$, where D is the total number of samples.

Consequently, $\boldsymbol{M}(s)$, the SI matrix function of the SbLR-BELBIC-PID controller shown in Fig. 4 is expressed by:

$$\boldsymbol{M}(s) = \begin{bmatrix} m_{11}(s) & \cdots & m_{1q}(s) \\ \vdots & \ddots & \vdots \\ m_{p1}(s) & \cdots & m_{pq}(s) \end{bmatrix}. \tag{1}$$

Each $m_{ij}(s)$ in the matrix represents a PID controller, which can be written as:

$$m_{ij}(s) = K_{P\ ij}^{SI}\left(1 + \frac{1}{K_{I\ ij}^{SI}s} + \frac{K_{D\ ij}^{SI}s}{1 + \left(\frac{K_{D\ ij}^{SI}}{N_{ij}^{SI}}\right)s}\right). \tag{2}$$

Here, $K_{P\ ij}^{SI} \in \mathbb{R}$ denotes the proportional gain, $K_{I\ ij}^{SI} \in \mathbb{R}$ the integral time, $K_{D\ ij}^{SI} \in \mathbb{R}$ the derivative gain, and $N_{ij}^{SI} \in \mathbb{R}$ the derivative filter coefficient, all associated with the SI. This formulation applies for $i = 1,\ 2,\ \dots, p$, and $j = 1,\ 2,\ \dots,\ q$. By taking the inverse

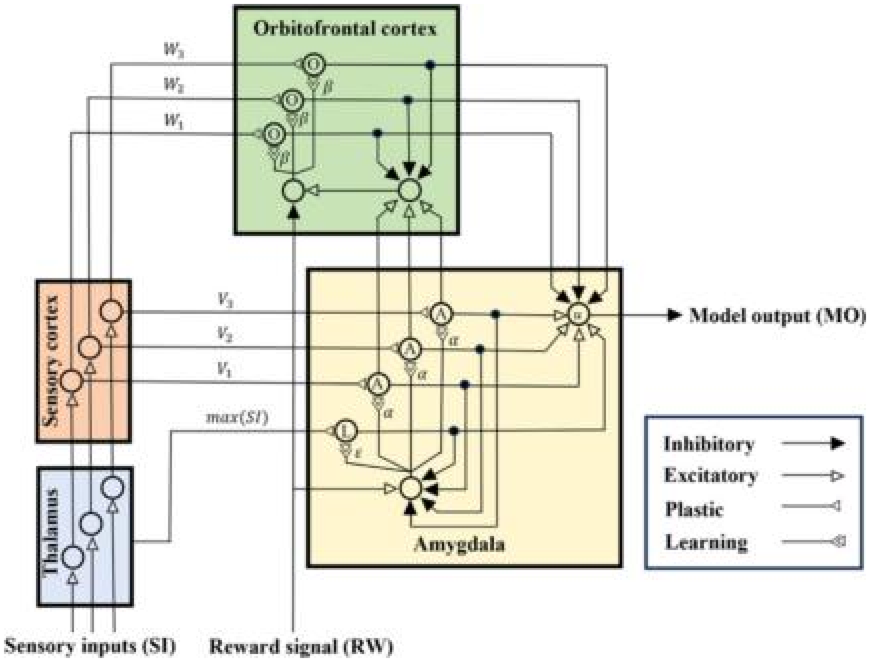

Fig. 3. Computational model of limbic system emotional learning [42].

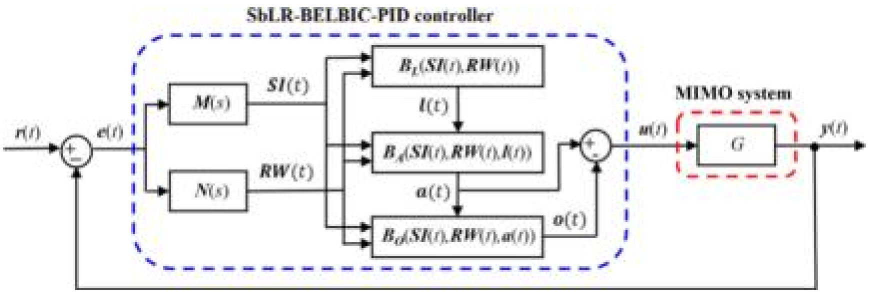

Fig. 4. Block diagram of the control system for the SbLR-BELBIC-PID controller.

Laplace transform, $m_{ij}(t) = \mathcal{L}^{-1}\{m_{ij}(s)\}$. Subsequently, the output of the SI signal for each individual element is expressed as:

$$SI_{ij}(t) = m_{ij}(t) \cdot e_j(t). \tag{3}$$

The error signal is defined as $e_j(t) = r_j(t) - y_j(t)$ for $j = 1, 2, \ldots, q$. In Eq. (3), $SI_{ij}(t)$ represents the (i, j)-th element of the SI matrix $\boldsymbol{SI}(t)$, and $e_j(t)$ corresponds to the j-th element of the error vector $\boldsymbol{e}(t)$.

Similarly, the SbLR-BELBIC-PID controller's RW matrix function $\boldsymbol{N}(s)$, as depicted in Fig. 4, is expressed as:

$$\boldsymbol{N}(s) = \begin{bmatrix} n_{11}(s) & \cdots & n_{1q}(s) \\ \vdots & \ddots & \vdots \\ n_{p1}(s) & \cdots & n_{pq}(s) \end{bmatrix}. \tag{4}$$

Each element $n_{ij}(s)$ is represented by a PID controller as:

$$n_{ij}(s) = K_{P\ ij}^{RW}\left(1 + \frac{1}{K_{I\ ij}^{RW} s} + \frac{K_{D\ ij}^{RW} s}{1 + \left(\frac{K_{D\ ij}^{RW}}{N_{ij}^{RW}}\right) s}\right). \tag{5}$$

In this formulation, $K_{P\ ij}^{RW} \in \mathbb{R}$ denotes the proportional gain, $K_{I\ ij}^{RW} \in \mathbb{R}$ the integral time, $K_{D\ ij}^{RW} \in \mathbb{R}$ the derivative gain, and $N_{ij}^{RW} \in \mathbb{R}$ the derivative filter coefficient for the RW controller. This applies for $i = 1, 2, \ldots, p$, and $j = 1, 2, \ldots, q$. Then, applying the inverse Laplace transform, each element is obtained as $n_{ij}(t) = \mathcal{L}^{-1}\{n_{ij}(s)\}$. The corresponding element of the RW signal matrix is then given by:

$$RW_{ij}(t) = n_{ij}(t) \cdot e_j(t). \tag{6}$$

In Eq. (6), $RW_{ij}(t)$ represents the (i,j)-th element of the RW signal matrix $\boldsymbol{RW}(t)$.

Then, the outputs of the SI and RW signals affect the computational model of emotional learning within the limbic system, specifically in the thalamus, amygdala, and orbitofrontal cortex [40,53] as illustrated in Fig. 3. Initially, as depicted in Fig. 4, the thalamus node in the SbLR-BELBIC-PID controller is represented by the matrix function $\boldsymbol{B_L}(\boldsymbol{SI}(t), \boldsymbol{RW}(t))$, which is expressed as

$$\boldsymbol{B_L}(\boldsymbol{SI}(t),\ \boldsymbol{RW}(t)) = \begin{bmatrix} l_{11}(t) & \cdots & l_{1q}(t) \\ \vdots & \ddots & \vdots \\ l_{p1}(t) & \cdots & l_{pq}(t) \end{bmatrix}. \tag{7}$$

The element-wise output of the thalamus node is defined as:

$$l_{ij}(t) = \max\ \left(SI_{ij}(t)\right) \cdot H_{ij}(t), \tag{8}$$

where $l_{ij}(t)$ is the (i,j)-th elements of the thalamus output matrix $\boldsymbol{l}(t)$. Within the thalamus node, $H_{ij}(t)$ in represents the (i,j)-th element of the plastic connection weight, which is calculated as:

$$H_{ij}(t) = \sum \Delta h_{ij}(t)dt + H_{ij}(0), \tag{9}$$

where $H_{ij}(0)$ specifies the initial value of $H_{ij}(t)$. The update in plastic connection weight $\Delta h_{ij}(t)$ is given by:

$$\Delta h_{ij}(t) = \tilde{\varepsilon}_{ij}(t) \cdot SI_{ij}(t) \cdot \max\left(0,\ RW_{ij}(t) - l_{ij}(t)\right). \tag{10}$$

For the thalamus node, the proposed adaptive emotional learning rate $\tilde{\varepsilon}_{ij}(t)$ in Eq. (10) is defined for $i = 1, 2, \ldots, p$, and $j = 1, 2, \ldots, q$. Further details of the adaptive emotional learning rate $\tilde{\varepsilon}_{ij}(t)$ will be provided in Section 3.

Next, as shown in Fig. 4, the amygdala node in the SbLR-BELBIC-PID controller is represented by the matrix function $\boldsymbol{B_A}(\boldsymbol{SI}(t),\ \boldsymbol{RW}(t),\ \boldsymbol{l}(t))$, which is defined as:

$$\boldsymbol{B_A}(\boldsymbol{SI}(t),\ \boldsymbol{RW}(t),\ \boldsymbol{l}(t)) = \begin{bmatrix} a_{11}(t) & \cdots & a_{1q}(t) \\ \vdots & \ddots & \vdots \\ a_{p1}(t) & \cdots & a_{pq}(t) \end{bmatrix}. \tag{11}$$

This matrix represents the output of the amygdala node signals, computed element-wise, and is expressed as:

$$a_{ij}(t) = SI_{ij}(t) \cdot V_{ij}(t), \tag{12}$$

where the element $a_{ij}(t)$ in the matrix $\boldsymbol{a}(t)$ of the amygdala, the node output signal corresponds to the (i,j)-th elements. Then, the amygdala plastic connection (i,j)-th elements, denoted by $V_{ij}(t)$ in Eq. (12), is expressed as:

$$V_{ij}(t) = \sum \Delta v_{ij}(t)dt + V_{ij}(0), \tag{13}$$

where $V_{ij}(0)$ is the initial value. The increment in the plastic weight, $\Delta v_{ij}(t)$, is calculated as:

$$\Delta v_{ij}(t) = \tilde{\alpha}_{ij}(t) \cdot SI_{ij}(t) \cdot \max\left(0,\ RW_{ij}(t) - a_{ij}(t) - l_{ij}(t)\right). \tag{14}$$

In Eq. (14), $\tilde{\alpha}_{ij}(t)$ represents the proposed adaptive learning rate for the amygdala, where $i = 1, 2, \ldots, p$, and $j = 1, 2, \ldots, q$. Further details on $\tilde{\alpha}_{ij}(t)$ are provided in Section 3. In Eq. (14), the max function plays an essential role in maintaining the monotonicity of the emotional learning process. It ensures the amygdala's plastic connection weight is always non-decreasing. This principle reflects the amygdala's inability to reverse the learning of an emotional signal once it has been established [40].

Then, as illustrated in Fig. 4, the orbitofrontal cortex node in the SbLR-BELBIC-PID controller is represented by the matrix function $\boldsymbol{B_O}(\boldsymbol{SI}(t),\ \boldsymbol{RW}(t),\ \boldsymbol{a}(t))$, defined as:

$$\boldsymbol{B_O}(\boldsymbol{SI}(t),\ \boldsymbol{RW}(t),\ \boldsymbol{a}(t)) = \begin{bmatrix} o_{11}(t) & \cdots & o_{1q}(t) \\ \vdots & \ddots & \vdots \\ o_{p1}(t) & \cdots & o_{pq}(t) \end{bmatrix}. \tag{15}$$

This matrix corresponds to the element-wise output of the orbitofrontal cortex node signals and is expressed as:

$$o_{ij}(t) = SI_{ij}(t) \cdot W_{ij}(t). \tag{16}$$

Here, the matrix $\boldsymbol{o}(t)$ contains the output signals of the orbitofrontal cortex node, with $o_{ij}(t)$ representing its (i,j)-th element. The corresponding plastic connection weight $W_{ij}(t)$ is given by:

$$W_{ij}(t) = \sum \Delta w_{ij}(t)dt + W_{ij}(0), \tag{17}$$

where $W_{ij}(0)$ denotes the initial value. Next, the weight update $\Delta w_{ij}(t)$ is computed by:

$$\Delta w_{ij}(t) = \tilde{\beta}_{ij}(t) \cdot SI_{ij}(t) \cdot \left(a_{ij}(t) - o_{ij}(t) - RW_{ij}(t)\right). \tag{18}$$

In Eq. (18), $\tilde{\beta}_{ij}(t)$ represents the adaptive learning rate of the orbitofrontal cortex for $i = 1, 2, \ldots, p$, and $j = 1, 2, \ldots, q$. A detailed description of $\tilde{\beta}_{ij}(t)$ is provided in Section 3.

Finally, the SbLR-BELBIC-PID controller's output signal vector that was used to control the MIMO systems in Fig. 4 can be expressed as:

$$\boldsymbol{u}(t) = \left[\sum_{j=1}^{q} a_{1j} - o_{1j},\ \sum_{j=1}^{q} a_{2j} - o_{2j},\ \ldots,\ \sum_{j=1}^{q} a_{pj} - o_{pj}\right]^T. \tag{19}$$

As a result, the control input energy for the MIMO systems, $\boldsymbol{u}(t) \in \mathbb{R}^p$ represented as $\boldsymbol{u}(t) = [u_1(t),\ u_2(t),\ \ldots,\ u_p(t)]^T$, is generated by the SbLR-BELBIC-PID controller's output. Following this, the performance in MIMO systems of the SbLR-BELBIC-PID controller is evaluated using the following indices:

$$\bar{e}_j = \int_{t_0}^{t_f} \left| r_j(t) - y_j(t) \right|^2 dt \tag{20}$$

$$\bar{u}_i = \int_{t_0}^{t_f} \left| u_i(t) \right|^2 dt \tag{21}$$

where $r_j(t)$, $y_j(t)$ and $u_i(t)$ correspond to the j-th and i th elements of the vectors $\boldsymbol{r}(t)$, $\boldsymbol{y}(t)$, and $\boldsymbol{u}(t)$, respectively. The assessment duration is defined within the interval $[t_0,\ t_f]$, where $t_0 \in \{0\} \cup \mathbb{R}_+$ and $t_f \in \mathbb{R}_+$. The tracking performance is measured by the integral of the squared difference between the reference input $\boldsymbol{r}(t)$ and the actual output $\boldsymbol{y}(t)$, denoted as $\bar{e}_j$ in Eq. (20). Our main objective is to minimize this variation. Additionally, the control effort is assessed through the integral of the squared input, $\bar{u}_i$ in Eq. (21), with the objective of keeping its magnitude as low as possible. This dual-objective design balances tracking performance and control effort, enabling accurate system response without excessive control input. The inclusion of both indices improves the practicality of the controller for real-world systems where actuator limitations or energy efficiency are critical design considerations. The adoption of these performance indices is widely recognized in various data-driven control studies for their effectiveness in enhancing the control accuracy of MIMO systems [12,62].

Furthermore, the SbLR-BELBIC-PID controller for MIMO systems uses a data-driven approach to define the fitness function as:

$$J = \sum_{j=1}^{q} w_{1j} \cdot \bar{e}_j + \sum_{i=1}^{p} w_{2i} \cdot \bar{u}_i, \tag{22}$$

where $w_{1j} \in \mathbb{R}(j = 1, 2, \ldots, q)$ weight the outputs, and $w_{2i} \in \mathbb{R}(i = 1, 2, \ldots, p)$ weight the control inputs. To ensure a fair evaluation, the weights are chosen to match those used in the baseline controller for comparison. As indicated by the right side of Eq. (22), the performance of the control system is assessed based on both the total integral of the squared input and the total integral of the squared error.

Next, based on the data-driven control framework, the problem associated with the SbLR-BELBIC-PID controller is outlined as follows:

Problem 2.1. Given the input and output data based on the control system block diagram in Fig. 4, determine $\boldsymbol{M}(s), \boldsymbol{N}(s), \boldsymbol{B_L}(\boldsymbol{SI}(t),\ \boldsymbol{RW}(t)), \boldsymbol{B_A}(\boldsymbol{SI}(t),\ \boldsymbol{RW}(t),\ \boldsymbol{l}(t))$, and $\boldsymbol{B_O}(\boldsymbol{SI}(t),\ \boldsymbol{RW}(t),\ \boldsymbol{a}(t))$ for the SbLR-BELBIC-PID controller such that the fitness function J in Eq. (22) is minimized.

3. Adaptive emotional learning rates for SbLR-BELBIC-PID controller design

In this section, the formulation of the proposed sigmoid-based functions emotional learning rates for the SbLR-BELBIC-PID is explained. The main objective is to substitute the constant emotional learning rates in the original BELBIC-PID with adaptive rates that vary according to the dynamics of the error signal. This modification is expected to enhance the appropriateness of the emotional learning responses. In the original BELBIC-PID controller, the learning rates for the thalamus, amygdala, and orbitofrontal cortex are denoted as ε, α, and β, respectively, as shown in Fig. 3. These learning rates remain constant throughout the simulation period. By keeping these learning rates constant, the overall emotional learning process is compromised. In particular, these rigid emotional learning rates limit the flexibility of the limbic system's emotional learning process in responding to error signals. Consequently, this may degrade overall control accuracy. Therefore, to solve the above issues, improved adaptive learning rates for the thalamus, amygdala, and orbitofrontal cortex were proposed, which are denoted as $\tilde{\varepsilon}_{ij}(t)$, $\tilde{\alpha}_{ij}(t)$, and $\tilde{\beta}_{ij}(t)$, respectively, as shown in the following equations:

$$\tilde{\varepsilon}_{ij}(t) = \varepsilon_{\min\ ij} - \left| \frac{\varepsilon_{\max\ ij} - \varepsilon_{\min\ ij}}{1 + e^{-\sigma_{ij}\left|e_j(t)\right|}} \right|, \tag{23}$$

$$\tilde{\alpha}_{ij}(t) = \alpha_{\min\ ij} - \left| \frac{\alpha_{\max\ ij} - \alpha_{\min\ ij}}{1 + e^{-\gamma_{ij}\left|e_j(t)\right|}} \right|, \tag{24}$$

and

$$\tilde{\beta}_{ij}(t) = \beta_{\min\ ij} - \left| \frac{\beta_{\max\ ij} - \beta_{\min\ ij}}{1 + e^{-\zeta_{ij}\left|e_j(t)\right|}} \right|. \tag{25}$$

In Eqs. (23)–(25), $\varepsilon_{\max\ ij}$, $\alpha_{\max\ ij}$, $\beta_{\max\ ij}$ represents the upper bounds, while $\varepsilon_{\min\ ij}$, $\alpha_{\min\ ij}$, $\beta_{\min\ ij}$ denotes the lower bounds for the adaptive learning rates of the amygdala, orbitofrontal cortex, and thalamus in the SbLR-BELBIC-PID controller, respectively. Additionally, the coefficients σ_{ij}, γ_{ij}, and ζ_{ij} are constants that adjust the sharpness of the transition between the upper and lower bounds. The notation $e_j(t)$ represents the error signal function between $r_j(t)$ and $y_j(t)$, as shown in Fig. 4. It is important to note that $\tilde{\varepsilon}_{ij}(t)$, $\tilde{\alpha}_{ij}(t)$, and $\tilde{\beta}_{ij}(t)$ in Eqs. (23)-(25) vary with the error signal and are not constant during the simulation. For simplicity in parameter tuning, we define $\Delta\varepsilon_{ij} = |\varepsilon_{\max\ ij} - \varepsilon_{\min\ ij}|$, $\Delta\alpha_{ij} = |\alpha_{\max\ ij} - \alpha_{\min\ ij}|$, and $\Delta\beta_{ij} = |\beta_{\max\ ij} - \beta_{\min\ ij}|$.

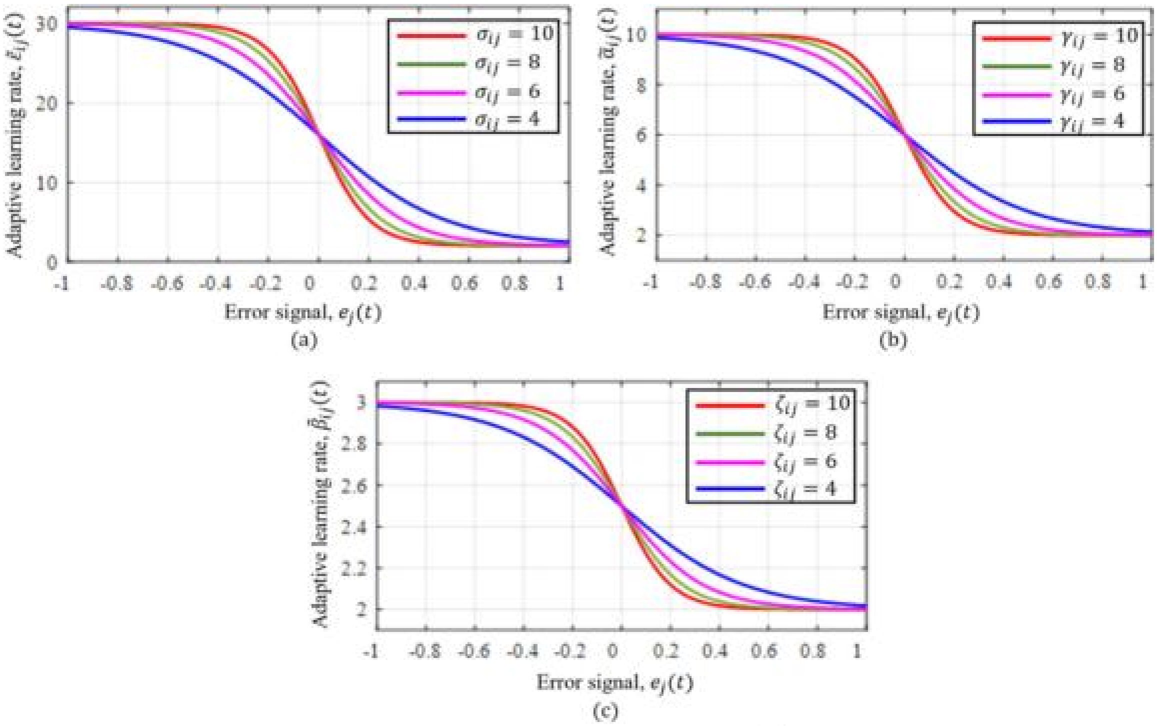

Fig. 5. Responses of adaptive learning rate (a) $\tilde{\varepsilon}_{ij}(t)$, (b) $\tilde{\alpha}_{ij}(t)$ and (c) $\tilde{\beta}_{ij}(t)$ with respect to the error signal.

The sigmoid-based function, or S-shaped curve, was derived from a series of ramp functions [63]. In this study, the SbLR-BELBIC-PID controller's emotional learning rates were modulated according to the error signal magnitude using a sigmoid-based function. For instance, large error signals require higher learning rates to enhance emotional learning responsiveness, while smaller error signals benefit from moderate learning rates to maintain appropriate emotional responses. Furthermore, Fig. 5(a), (b), and (c) illustrate examples of adaptive emotional learning rates for $\tilde{\varepsilon}_{ij}(t)$, $\tilde{\alpha}_{ij}(t)$, and $\tilde{\beta}_{ij}(t)$, corresponding to the error signal $e_j(t)$ for different values of σ_{ij}, γ_{ij}, and ζ_{ij}, respectively. The proposed sigmoid function enables the learning rates to adapt smoothly based on the error signal within the specified bounds of $\Delta\varepsilon_{ij}$, $\Delta\alpha_{ij}$, and $\Delta\beta_{ij}$. Moreover, Fig. 5(a), (b), and (c) also show the different ranges of these learning rates bounds, from large to moderate and small, respectively. These variation ranges of bounds demonstrated different system behaviors that required well-regulated emotional learning rates to prevent undesirable emotional responses. For instance, a less sensitive system control may be more appropriate with larger learning rate bounds, as shown in Fig. 5(a), to enhance the emotional learning responses. In contrast, a more sensitive system may benefit from smaller learning rate bounds, as shown in Fig. 5(c), to mitigate excessive emotional responses. Meanwhile, the constant parameters σ_{ij}, γ_{ij}, and ζ_{ij} were employed to adjust the sharpness of the adaptive learning rate transitions between the upper and lower bounds. In these figures, higher values of parameters σ_{ij}, γ_{ij}, and ζ_{ij} increased the transition sharpness of the lower and upper learning rates bounds, and vice versa. This contributes to enhancing the rates at which the plastic connection weights of the limbic system were updated in response to the error signals, as referenced in Eqs. (10), (14), and (18). Consequently, this improvement enhanced the SbLR-BELBIC-PID controller's flexibility by improving the quality of its emotional learning responses. As a result, the proposed method enhances the control accuracy and overall performance of the SbLR-BELBIC-PID in managing complex MIMO systems.

3.1. Stability analysis of the SbLR-BELBIC-PID controller

The stability of the proposed SbLR-BELBIC-PID controller is analyzed in terms of boundedness of its internal emotional learning dynamics. This analysis focuses on the adaptive learning mechanism and controller structure, which is consistent with the adopted data-driven control framework and does not require explicit knowledge of nonlinear MIMO plant dynamics.

Assumption 1. The reference signals $\boldsymbol{r}(t)$ and the plant outputs $\boldsymbol{y}(t)$ are bounded within the operating region considered. Consequently, the tracking error signals $\boldsymbol{e}(t) = \boldsymbol{r}(t) - \boldsymbol{y}(t)$ are bounded.

Assumption 2. The sensory input $\mathrm{SI}_{ij}(t)$ and reward signal $\mathrm{RW}_{ij}(t)$ defined in Eqs. (2) and (5) are generated using PID-based error signals. Therefore, bounded tracking error signals $e_j(t)$ implies that $\mathrm{SI}_{ij}(t)$ and $\mathrm{RW}_{ij}(t)$ remain bounded.

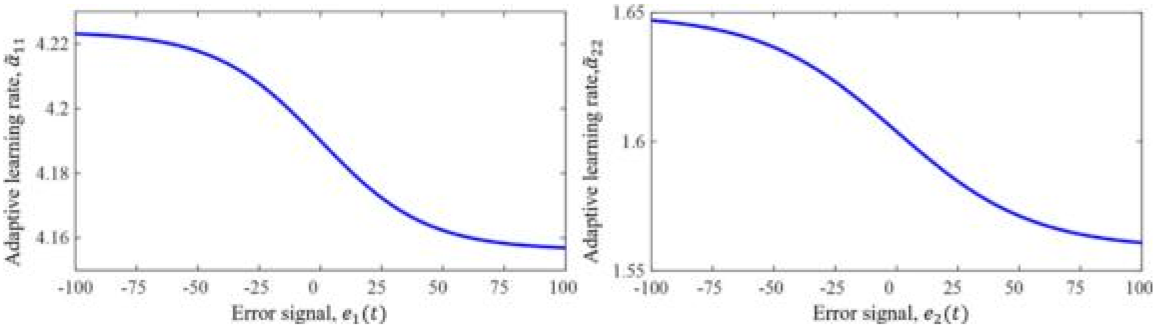

Fig. 6. SbLR-based emotional learning rates for (a) amygdala α_{11} and (b) amygdala α_{22} in partial SbLR-BELBIC-PID (Condition 1).

Assumption 3. The sigmoid-based adaptive learning rates defined in Eqs. (23)–(25) are bounded for all t such that $\tilde{\varepsilon}_{ij}(t) \in [\varepsilon_{\min\ ij}, \varepsilon_{\max\ ij}]$, $\tilde{\alpha}_{ij}(t) \in [\alpha_{\min\ ij}, \alpha_{\max\ ij}]$, and $\tilde{\beta}_{ij}(t) \in [\beta_{\min\ ij}, \beta_{\max\ ij}]$.

Lemma 1. Under Assumption 3, the adaptive learning rates $\tilde{\varepsilon}_{ij}(t)$, $\tilde{\alpha}_{ij}(t)$ and $\tilde{\beta}_{ij}(t)$ are bounded for all t.

Proof. This follows directly from the bounded range of the sigmoid functions and the finite limits $\varepsilon_{\min\ ij}, \varepsilon_{\max\ ij}$, $\alpha_{\min\ ij}, \alpha_{\max\ ij}$, $\beta_{\min\ ij}$ and $\beta_{\max\ ij}$.

Lemma 2. Under Assumptions 1–3, the plastic connection weight-update rates $\Delta h_{ij}(t)$, $\Delta v_{ij}(t)$, and $\Delta w_{ij}(t)$ defined in Eqs. (10), (14), and (18) are bounded for all t.

Proof. From Assumptions 1 and 2, $\mathrm{SI}_{ij}(t)$ and $\mathrm{RW}_{ij}(t)$ are bounded. From Lemma 1, the adaptive learning rates are bounded. Since the update laws in Eqs. (10), (14), and (18) are composed of products of bounded signals, the corresponding weight-update rates remain bounded for all t.

Define the aggregated weight vector $\theta(t) = \mathrm{vec}\{H(t), V(t), W(t)\}$,which collects all thalamus, amygdala, and orbitofrontal cortex weights. Consider the Lyapunov candidate function $\mathcal{V}_L(t) = \frac{1}{2} \parallel \theta(t) \|^2$, where $\theta(t)$ denotes the adaptive weight vector. Taking the time derivative yields $\mathcal{V}_L(t) = \theta^{\mathrm{T}}(t)\,\theta(t)$. From Eqs. (9), (13), and (17), $\theta(t)$ consists of bounded weight-update terms $\Delta h_{ij}(t)$, $\Delta v_{ij}(t)$, and $\Delta w_{ij}(t)$. Therefore, there exist positive constant c_1 and $c_2$such that $\mathcal{V}_L(t) \le c_1 \parallel \theta(t) \parallel + c_2$. This inequality implies that the internal emotional learning dynamics are uniformly ultimately bounded. Consequently, the plastic weights $H_{ij}(t)$, $V_{ij}(t)$, and $W_{ij}(t)$ remain bounded within the operating region considered, which is consistent with standard Lyapunov-based boundedness results reported in adaptive neural and learning-based control systems [64,65].

Corollary 1. Under Assumptions 1–3, the controller output $\boldsymbol{u}(t)$ defined in Eq. (19) is bounded.

Proof. From Eqs. (12) and (16), the amygdala output $a_{ij}(t) = SI_{ij}(t) \cdot V_{ij}(t)$ and orbitofrontal cortex output $o_{ij}(t) = SI_{ij}(t) \cdot W_{ij}(t)$ are products of bounded signals and bounded weights. Hence, both $a_{ij}(t)$ and $o_{ij}(t)$ are bounded, which implies that the control input $\boldsymbol{u}(t)$ remains bounded.

Remark 3.1. The proposed SbLR-BELBIC-PID controller is formulated within a data-driven control framework and is applied to nonlinear MIMO systems without requiring explicit knowledge of plant dynamics. Accordingly, the stability analysis is intentionally confined to the internal emotional learning mechanism and controller structure rather than global closed-loop plant stability. The presented Lyapunov-based analysis establishes boundedness of the adaptive learning rates, weight-update dynamics, and controller output under bounded operating signals [66]. This analysis does not aim to establish global or asymptotic stability of an arbitrary nonlinear MIMO plant, which would require explicit plant modeling assumptions that are inconsistent with the adopted data-driven control framework. Instead, stability is interpreted in terms of practical boundedness of the learning dynamics and control action.

3.2. Preliminary ablation study of partial SbLR-BELBIC-PID controller

As part of the preliminary study, the effect of the SbLR on the learning rate of each BELBIC component was examined to assess its influence on the performance of the SbLR-BELBIC-PID controller. The ablation test was performed using the Twin Rotor MIMO System (TRMS) plant, as described in Section 5.1, and the results were benchmarked against those of the standard BELBIC-PID controller [58]. Three testing conditions were considered. In Condition 1, SbLR was applied only to the amygdala, while the orbitofrontal cortex and thalamus operated with constant learning rates. In Condition 2, SbLR was applied exclusively to the orbitofrontal cortex, with the amygdala and thalamus using constant learning rates. In Condition 3, SbLR was applied only to the thalamus, while the amygdala and orbitofrontal cortex retained constant learning rates. To ensure a fair comparison, identical weighting factors were employed across all three conditions and the benchmark model [58]. Figs. 6–8 present the SbLR-based emotional learning rates for Conditions 1, 2, and 3, respectively, while Table 1 summarizes the numerical performance indices for all conditions. The results indicate that

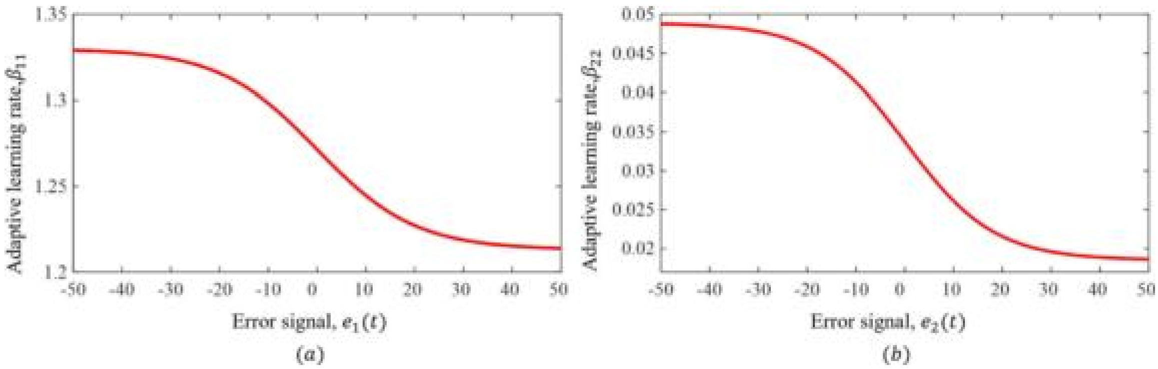

Fig. 7. SbLR-based emotional learning rates for (a) orbitofrontal cortex β_{11} and (b) orbitofrontal cortex β_{22} in partial SbLR-BELBIC-PID (Condition 2).

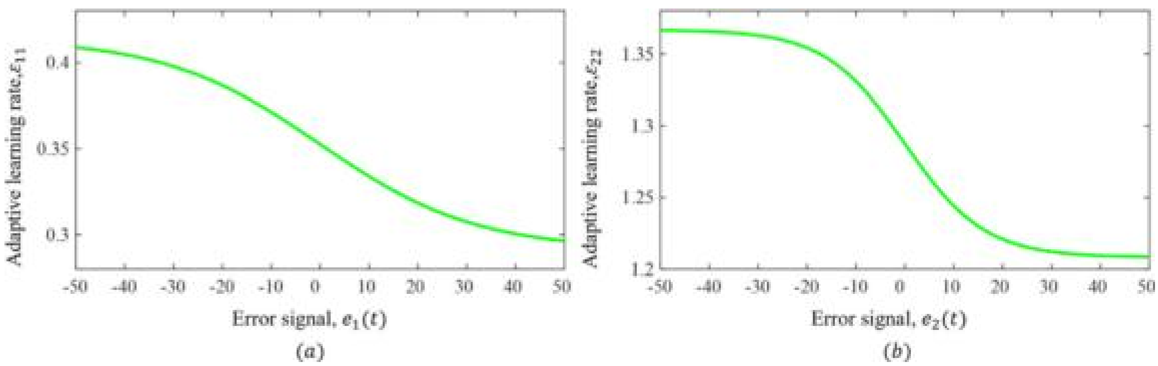

Fig. 8. SbLR-based emotional learning rates for (a) thalamus ε_{11} and (b) thalamus ε_{22} in partial SbLR-BELBIC-PID (Condition 3).

Table 1
Numerical results of partial SbLR-BELBIC-PID ablation tests on the Twin Rotor MIMO System (TRMS).

Performance Index	BELBIC-PID [58]	Condition 1	Condition 2	Condition 3
Fitness function J	176.2902	175.9149	186.3242	**175.5036**
ISE $\sum_{j=1}^{2} \bar{e}_j$	0.1184	0.1205	0.1226	**0.1154**
ISI $\sum_{i=1}^{2} \bar{u}_i$	44.2307	**41.4414**	49.3839	46.2541

Condition 1 improved the fitness function and ISI but increased the ISE. Furthermore, Condition 2 produced inferior performance across all indices, whereas Condition 3 improved the fitness function and ISE but increased the ISI. These findings indicate that the amygdala and thalamus are more responsive to SbLR adaptation than the orbitofrontal cortex, with the thalamus providing the most significant improvement as reflected by the lowest fitness function value. Consequently, the observed advantages of partial SbLR application suggest that simultaneous adaptation across all BELBIC components can better exploit their complementary strengths and lead to balanced improvements in control performance.

The observed performance trends can be interpreted by examining the functional roles of individual BELBIC components within the controller structure. The amygdala primarily governs excitatory emotional learning and directly influences the magnitude of the control signal. When the sigmoid based learning rate is applied only to the amygdala, control effort is reduced, as reflected by the lower ISI; however, tracking accuracy slightly degrades, as indicated by the increased ISE, due to limited adaptive regulation. The orbitofrontal cortex mainly provides inhibitory regulation, and exclusive adaptation of this component disrupts the balance between excitation and inhibition, leading to inferior overall control performance. In contrast, applying the adaptive learning rate to the thalamus enhances sensory filtering and increases the salience of dominant error signals, resulting in reduced ISE at the cost of increased control effort. These results confirm that each BELBIC component contributes differently to tracking accuracy and control energy. Therefore, coordinated sigmoid based learning rate adaptation applied simultaneously across all BELBIC components is more effective in achieving balanced control performance.

4. SbLR-BELBIC-PID controller tuning using modified safe experimentation dynamics algorithm

In this section, the procedure to tune the SbLR-BELBIC-PID controller described in Sections 2 and 3 is explained. Firstly, a brief overview of the safe experimentation dynamics algorithm (SEDA) is provided. Next, a modified version of SEDA (MSEDA) is described to solve the local optimal issue of the original SEDA. As mentioned previously [58], the earlier version of the MSEDA has been reported. Finally, the SbLR-BELBIC-PID controller is implemented using the MSEDA-based data-driven approach, with the goal of minimizing the control objective specified in Eq. (22).

4.1. Overview of safe experimentation dynamics algorithm (SEDA)

The safe experimentation dynamics algorithm (SEDA) introduced by [67] is inspired by game-theoretic principles, specifically within the framework of weakly acyclic games. In such games, players make simultaneous strategy selections from a finite set of available options, with their decisions influenced by a strategy adjustment process. This process outlines how players choose strategies at each stage using the information that they gathered from earlier stages. The goal of SEDA is to achieve an optimal equilibrium in games with common interests by maximizing the utility of each player. Previous works have successfully applied SEDA as a data-driven tool to address optimization problems in controller parameter tuning, as demonstrated in [68,69].

To provide more details on SEDA, the optimization problem is stated as:

$$\min_{\boldsymbol{x}(k)\in\mathbb{R}^n} f(\boldsymbol{x}(k)) \tag{26}$$

where $f : \mathbb{R}^n \to \mathbb{R}$ represents the fitness function, and $\boldsymbol{x}(k) \in \mathbb{R}^n$ denotes the design parameters at the iteration k. The problem outlined in Eq. (26) is to iteratively update the parameters until the maximum iteration k_{max} is reached, to find the optimal solution $\boldsymbol{x}_{opt} \in \mathbb{R}^n$. The revised rule for SEDA is described by:

$$x_i(k+1) = \begin{cases} h(\gamma),\ if\ rv_1 < E, \\ \bar{x}_i,\ if\ rv_1 \geq E. \end{cases} \tag{27}$$

Here, $\gamma = (\bar{x}_i - K_g \cdot rv_2)$, where $h(\gamma)$ denotes a new candidate solution generated by modifying the current one, and γ defines the perturbation parameters. For iterations $k = 1,\ 2 \ldots k_{max}$, the index $x_i \in \mathbb{R}$ corresponds to the i-th element of the design vector $\boldsymbol{x} \in\ \mathbb{R}^n$, while $\bar{x}_i \in \mathbb{R}$ corresponds to the i-th element of the current optimal design vector $\bar{\boldsymbol{x}} \in\ \mathbb{R}^n$. The scalar value K_g represents the step interval for random variations in $x_i \in \mathbb{R}$**,** while E indicates the probability of selecting new design parameters for $\boldsymbol{x}(k)$. The values $rv_1 \in \mathbb{R}$ and $rv_2 \in \mathbb{R}$ are random numbers: $rv_1$is chosen uniformly from the range $[0, 1]$, while rv_2 is randomly selected within the bounds x_{min} and x_{max}. Following this, as defined in Eq. (27), the update function $h(\gamma)$ is given by:

$$h(\gamma) = \begin{cases} x_{max},\ \gamma > x_{max}, \\ \gamma,\ x_{min} \leq \gamma \leq x_{max}, \\ x_{\min},\ \ \gamma < x_{min}. \end{cases} \tag{28}$$

4.2. Modified safe experimentation dynamics algorithm (MSEDA)

The optimal controller design parameters have been successfully obtained using the original SEDA method as a data-driven tool. However, certain limitations are present. In Eq. (27), the original SEDA updates rely on a fixed probability E, which restricts flexibility by preventing dynamic control of exploration and exploitation. Emphasizing exploration excessively can weaken exploitation, making it crucial to maintain an appropriate balance between these two phases. To resolve this issue, MSEDA introduces a new probability expression. The new probability expression has been reported in our previous paper in [58], which is given by:

$$E(k) = 1 - \lambda, \tag{29}$$

where $\lambda = (\frac{K_e \cdot k}{k_{max}})$. Here, as the iteration k increases, the scaling factor λ also increases. As a result, the probability $E(k)$ decreases as the iterations progress. The value of the new probability coefficient, denoted as K_e, is set to be <1. Then, using the updated probability coefficient in MSEDA, the next iteration is computed as:

$$x_i(k+1) = \begin{cases} h(\gamma),\ if\ rv_1 < E(k), \\ \bar{x}_i,\ if\ rv_1 \geq E(k). \end{cases} \tag{30}$$

Based on the updated MSEDA equation, the probability $E(k)$ is large during the initial phase of the iteration, resulting in more design parameter elements being updated. During this phase, the algorithm must explore the search space extensively to minimize the risk of becoming trapped in local optima. The probability decreases as the iteration progresses (when k is large), resulting in fewer design parameter elements being perturbed. At this point, the algorithm should focus on intensifying the search in promising regions of the solution space to refine the results and identify better solutions. The effectiveness of this approach was confirmed in [58], where it served as a data-driven optimization method to tune the standard BELBIC-PID across several MIMO systems. Additionally, the MSEDA flowchart in Fig. 9 outlines the algorithm's process.

Remark 4.2. It is important to note that x_{min} and x_{max} define the lower and upper bounds of the design parameters, respectively. These boundaries were established through several preliminary experiments with the optimization problem. The selection of values

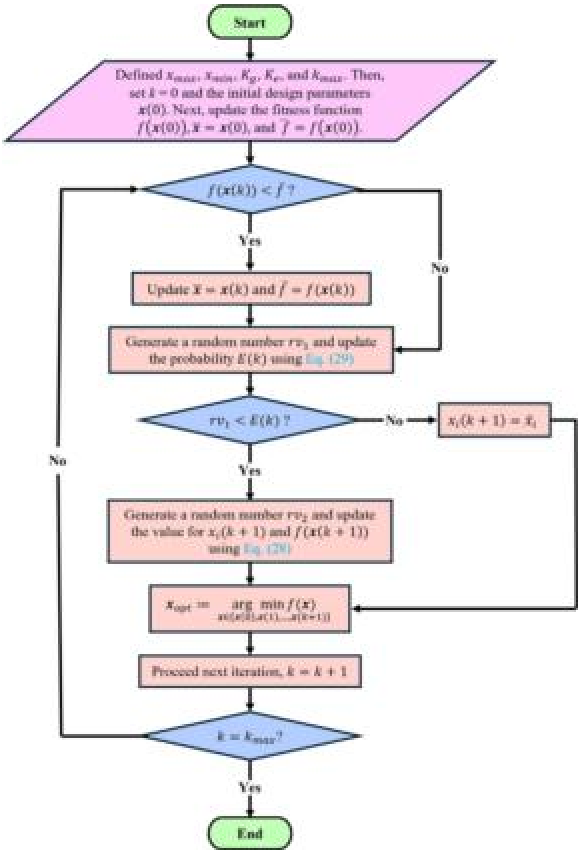

Fig. 9. Flowchart of MSEDA.

for K_g and K_e follows the guidelines in [67] and [58]. In particular, for any probability $E(k) < 1$, a sufficiently small exploration rate K_g ensures that the optimal solution $\boldsymbol{x}_{opt}$ is reached after a sufficiently large number of iterations. This justifies the choice of a more considerable k_{max}, which guarantees convergence to the optimal solution. The maximum iteration k_{max} is usually chosen at the point where the convergence curve begins to flatten, indicating minimal improvement with additional iterations.

4.3. MSEDA-based data-driven optimization of SbLR-BELBIC-PID

This section presents the optimization process of the SbLR-BELBIC-PID controller using the MSEDA method, focusing on reducing the fitness function defined in Eq. (22). The optimization process begins by initializing the MSEDA solution vector for designing the SbLR-BELBIC-PID controller parameters, as stated in Eq. (31). This vector is given by:

$$\boldsymbol{\psi} = \left[\boldsymbol{K}_P^{SI},\ \boldsymbol{K}_I^{SI},\ \boldsymbol{K}_D^{SI},\ \boldsymbol{N}^{SI},\ \boldsymbol{K}_P^{RW},\ \boldsymbol{K}_I^{RW},\ \boldsymbol{K}_D^{RW},\ \boldsymbol{N}^{RW},\ \boldsymbol{\varepsilon},\ \boldsymbol{\alpha},\ \boldsymbol{\beta}, \boldsymbol{\sigma}, \boldsymbol{\gamma}, \boldsymbol{\zeta}, \Delta\boldsymbol{\varepsilon}, \Delta\boldsymbol{\alpha}, \Delta\boldsymbol{\beta}\right]^T \in \mathbb{R}^n, \tag{31}$$

with each element defined as $\psi_i = 10^{x_i}$ for $(i = 1, 2, \ldots, n)$. A logarithmic parameterization is employed to accelerate the search for optimal design parameters by improving numerical conditioning and facilitating faster convergence of the optimization process. This approach is particularly effective in tuning control parameters that span several orders of magnitude. It allows multiplicative changes in controller gains to be represented as additive updates in the log-domain variables x_i, which leads to a more balanced and efficient search behavior during the MSEDA-based optimization. Based on Eq. (30), each design parameter, $x_i(k)$, is iteratively updated to achieve optimal control performance. These updated design parameters are influenced by both the control input, $\boldsymbol{u}(t)$, and the control error, $\boldsymbol{e}(t)$, as defined in Eq. (22). Specifically, the changes of $\boldsymbol{\psi}$ will contribute to the changes of $J(\boldsymbol{\psi})$, which is based on the produced $\boldsymbol{u}(t)$ and $\boldsymbol{e}(t)$. Note that the fitness function $J(\boldsymbol{\psi})$ from Eq. (22) is evaluated alongside the fitness function defined in Eq. (26), expressed as $J(\boldsymbol{\psi}) = f(\boldsymbol{x})$. If the new fitness function value $f(\boldsymbol{x}(k))$ is better, it updates the value of $f(\bar{\boldsymbol{x}}(k))$ and the corresponding design parameters $\bar{\boldsymbol{x}}(k)$. The procedure for updating each design parameter $x_i(k)$ is described in detail in Section 4.2, followed by the tuning process for the controller's design parameters. This coordination between the MSEDA-based SbLR-BELBIC-PID controller and the MIMO systems is iterated until the maximum iteration k_{max} is reached. Finally, the optimal design parameters $\bar{\boldsymbol{x}}(k_{max})$ are recorded as $\boldsymbol{x}_{opt}$. Fig. 10 illustrates a comprehensive block diagram that outlines the tuning approach applied to the MSEDA-based SbLR-BELBIC-PID controller. The systematic procedure for optimizing the data-driven SbLR-BELBIC-PID controller is outlined as follows:

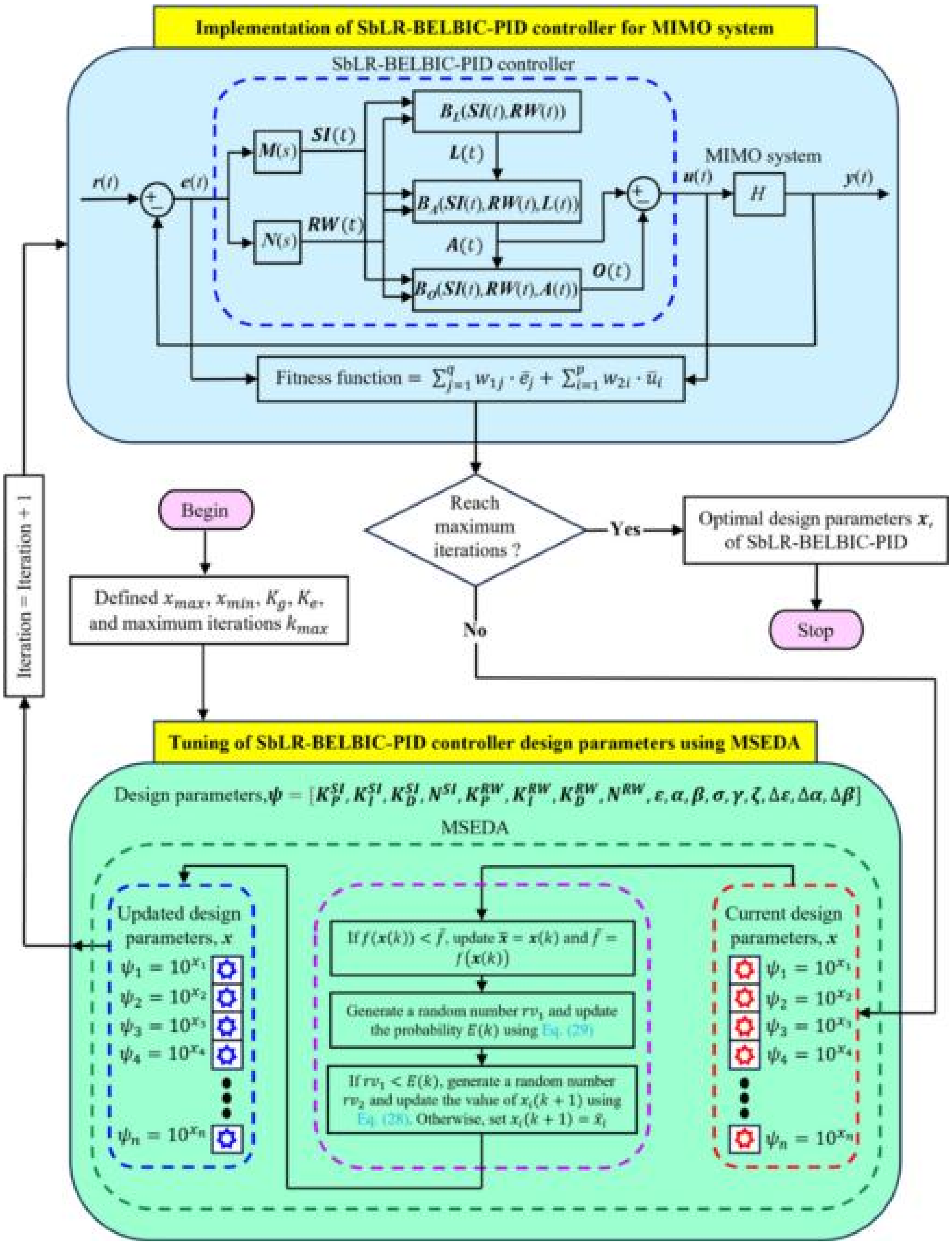

Fig. 10. MSEDA-based SbLR-BELBIC-PID controller implementation in a MIMO system.

Step 1: The initial design parameters are set as $x_i = \log \psi_i$ for $(i = 1, 2, \ldots, n)$, and the associated fitness function is defined as $f(\boldsymbol{x}) = J(\boldsymbol{K}_P^{SI}, \boldsymbol{K}_I^{SI}, \boldsymbol{K}_D^{SI}, \boldsymbol{N}^{SI}, \boldsymbol{K}_P^{RW}, \boldsymbol{K}_I^{RW}, \boldsymbol{K}_D^{RW}, \boldsymbol{N}^{RW}, \varepsilon, \boldsymbol{\alpha}, \boldsymbol{\beta}, \boldsymbol{\sigma}, \boldsymbol{\gamma}, \boldsymbol{\zeta}, \Delta\boldsymbol{\varepsilon}, \Delta\boldsymbol{\alpha}, \Delta\boldsymbol{\beta})$.Subsequently, optimization procedure then proceeds by specifying the maximum number of iterations, k_{max}.

Step 2: The MSEDA-based technique is used to compute the updated design parameters, as described in Eq. (30).

Step 3: Once the maximum iteration k_{max} is reached, the optimal design parameters are obtained as $\boldsymbol{x}_{opt} = \bar{\boldsymbol{x}}(k_{max})$. The optimal solution vector $\boldsymbol{\psi}_{opt} = [\ 10^{x_{1\,opt}}\quad 10^{x_{2\,opt}}\quad \cdots\ 10^{x_{n\,opt}}\ ]^T$ is subsequently applied to update the SbLR-BELBIC-PID controller, specifically by assigning the values to$\boldsymbol{M}(s)$, $\boldsymbol{N}(s)$, $\boldsymbol{B_L}(\boldsymbol{SI}(t), \boldsymbol{RW}(t))$, $\boldsymbol{B_A}(\boldsymbol{SI}(t), \boldsymbol{RW}(t), \boldsymbol{l}(t))$, and $\boldsymbol{B_O}(\boldsymbol{SI}(t), \boldsymbol{RW}(t), \boldsymbol{a}(t))$, as shown in Fig. 4.

Remark 4.3. It is important to note that the methods used in this paper are grounded in a data-driven control framework. Specifically, these methods rely solely on the measured input and output data to update the controller design parameters rather than using plant mathematical models. Therefore, it is impossible to rigorously demonstrate the stability of the closed-loop system using this approach. Thus, system stability is evaluated in this study by verifying that the output response converges to a steady state without divergence throughout the simulation period.

5. Numerical example

In this section, we evaluated the performance of the proposed SbLR-BELBIC-PID controller, which primarily aims to enhance the standard BELBIC-PID controller [58]. We evaluated the proposed controller on two MIMO systems, the TRMS, and the container gantry crane system, using a data-driven control framework to assess its effectiveness. The controller structures described in Sections 2 and 3 were implemented to control these systems. The MSEDA-based technique, detailed in Section 4, was then applied to tune the SbLR-BELBIC-PID controller design parameters. The performance of the SbLR-BELBIC-PID controller was evaluated and compared with the standard BELBIC-PID [58], NEPID [36], and PID [36] controllers, as presented in previous works. Furthermore, to assess robustness, an additional experiment was conducted under measurement noise, where the SbLR-BELBIC-PID was specifically compared with the standard BELBIC-PID to verify the effectiveness of the proposed adaptive learning rate in handling disturbances. The evaluation of each controller was carried out using the following criteria:

(i) The assessment of the fitness function $J(\boldsymbol{K}_{\boldsymbol{P}}^{\boldsymbol{SI}}, \boldsymbol{K}_{\boldsymbol{I}}^{\boldsymbol{SI}}, \boldsymbol{K}_{\boldsymbol{D}}^{\boldsymbol{SI}}, \boldsymbol{N}^{\boldsymbol{SI}}, \boldsymbol{K}_{\boldsymbol{P}}^{\boldsymbol{RW}}, \boldsymbol{K}_{\boldsymbol{I}}^{\boldsymbol{RW}}, \boldsymbol{K}_{\boldsymbol{D}}^{\boldsymbol{RW}}, \boldsymbol{N}^{\boldsymbol{RW}}, \boldsymbol{\varepsilon}, \boldsymbol{\alpha}, \boldsymbol{\beta}, \boldsymbol{\sigma}, \boldsymbol{\gamma}, \boldsymbol{\zeta}, \Delta\boldsymbol{\varepsilon}, \Delta\boldsymbol{\alpha}, \Delta\boldsymbol{\beta})$, the ISE $\sum_{j=1}^{q} \bar{e}_j$, and the ISI $\sum_{i=1}^{p} \bar{u}_i$.

(ii) The proposed SbLR-BELBIC-PID is assessed by comparing it with the standard BELBIC-PID. The percentage improvement in control accuracy $J_A(\boldsymbol{\psi})$ is calculated as:

$$\%\ J_A(\boldsymbol{\psi}) = \frac{\left| J(\boldsymbol{\psi})_{\text{SbLR-BELBIC-PID}} - J(\boldsymbol{\psi})_{\text{BELBIC-PID}} \right|}{J(\boldsymbol{\psi})_{\text{BELBIC-PID}}} \times 100\%. \tag{32}$$

(iii) The trajectory tracking robustness under noisy measurement, assessed using four integral error criteria: the Integral of Absolute Error (IAE), Integral of Squared Error (ISE), Integral of Time-weighted Absolute Error (ITAE), and Integral of Time-weighted Squared Error (ITSE), defined as:

$$\text{IAE} = \int_0^{t_f} \left| e_j(t) \right| dt, \tag{33}$$

$$\text{ISE} = \int_0^{t_f} e_j^2(t) dt, \tag{34}$$

$$\text{ITAE} = \int_0^{t_f} t \left| e_j(t) \right| dt, \tag{35}$$

$$\text{ITSE} = \int_0^{t_f} t e_j^2(t) dt, \tag{36}$$

where $e_j(t) = r_j(t) - y_j(t)$ for $j = 1, 2, \ldots, q$ denotes the tracking error between the reference signal and the measured output signal, and t_f represents the final time of the simulation.

Remark 5.1. To ensure a fair comparison, the proposed SbLR-BELBIC-PID controller and its standard counterpart were optimized using the MSEDA-based technique with identical algorithm coefficients and maximum iterations. In addition, identical performance indices and weighting coefficients were applied to tune the BELBIC-PID, NEPID, and PID controllers.

5.1. Example 1: twin rotor MIMO system (TRMS)

The TRMS is commonly employed as a benchmark to test the performance of controllers in nonlinear MIMO environments. It replicates helicopter behavior, enabling free rotation along a beam through yaw and pitch motions in horizontal and vertical planes. Two direct-current (DC) motors power the propellers, which are mounted at each end of the beam. The main and tail propellers produce lift for vertical movement and control horizontal rotation, respectively. As shown in Fig. 11, both DC motors drive the propellers independently. The horizontal response of the TRMS is represented by α_h, while the vertical response is denoted by α_v. The TRMS controls aerodynamic forces by adjusting the DC motor speed, which is driven by independent voltage inputs u_h and u_v. These inputs range from −1 to 1 and correspond to voltage levels between −5 V and 5 V, which regulate the speed of each propeller. The TRMS dynamics are represented as follows:

$$\boldsymbol{x}_a = \boldsymbol{f}\left(\boldsymbol{x}_a, \boldsymbol{u}\right) \tag{37}$$

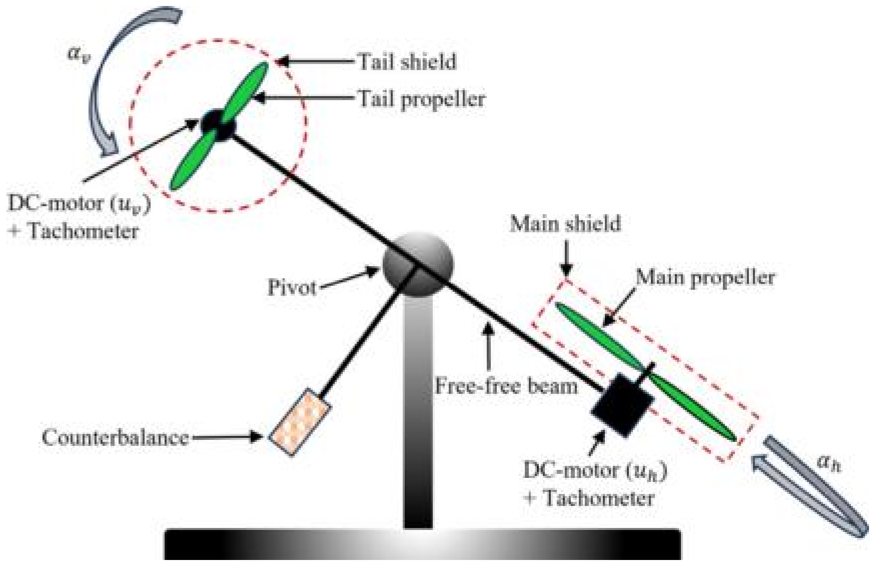

Fig. 11. The model of the TRMS.

and

$$y = C x_a \tag{38}$$

where $x_a = [\ \alpha_h \quad \alpha_v\ ]^T$ and $u = [\ u_h \quad u_v\ ]^T$.

Next

$$f(x_a, u) = \begin{bmatrix} \frac{s_h + J_{mr}\omega_m(i_v)\cos\alpha_v}{D\ \sin^2\alpha_v + E\ \cos^2\alpha_v + G} \\ 9.1\left(s_v + J_{tr}\omega_t(i_h)\right) \end{bmatrix} = \begin{bmatrix} \alpha_h \\ \alpha_v \end{bmatrix}, \tag{39}$$

where

$$s_h = l_t S_f F_h(\omega_t)\cos\alpha_v - k_h\alpha_h, \tag{40}$$

$$s_v = l_m S_f F_v(\omega_m) - g(0.0099\cos\alpha_v + 0.0168\sin\alpha_v - k_v\alpha_v - 0.0252\alpha^2\sin 2\alpha_v, \tag{41}$$

$$i_h = \frac{1}{T_{tr}}(u_h - i_h), \tag{42}$$

$$i_v = \frac{1}{T_{mr}}(u_v - i_v), \tag{43}$$

$$\omega_m(i_v) = 90.99 i_v{}^6 + 599.73 i_v{}^5 - 129.26 i_v{}^4 - 1283.64 i_v{}^3 + 63.45 i_v{}^2 + 1283.41 i_v, \tag{44}$$

$$\omega_t(i_h) = 2020 i_h{}^5 - 194.69 i_h{}^4 - 4283.15 i_h{}^3 + 262.27 i_h{}^2 + 3768.83 i_h, \tag{45}$$

$$F_v(\omega_m) = -3.48\times10^{-12}\omega_m{}^5 + 1.09\times10^{-9}\omega_m{}^4 + 4.123\times10^{-6}\omega_m{}^3 - 1.632\times10^{-4}\omega_m{}^2 + 9.544\times10^{-2}\omega_m \tag{46}$$

and

$$F_h(\omega_t) = -3\times10^{-14}\omega_t{}^5 - 1.595\times10^{-11}\omega_t{}^4 + 2.511\times10^{-7}\omega_t{}^3 - 1.808\times10^{-4}\omega_t{}^2 + 8.01\times10^{-2}\omega_t. \tag{47}$$

Following these, the TRMS horizontal and vertical position outputs can be expressed as:

$$y = \begin{bmatrix} 1 & 0 \\ 0 & 1 \end{bmatrix} = \begin{bmatrix} \alpha_h \\ \alpha_v \end{bmatrix}. \tag{48}$$

In Eq. (39), i_v refers to the armature current of the main propeller while i_h represents the armature current of the tail propeller. The angular velocities of the main and tail propellers are denoted by ω_m and ω_t, respectively. The forces F_v and F_h control the vertical and horizontal motions of the combined beam. Meanwhile, the angular momentum in the horizontal and vertical planes is represented

Table 2
TRMS parameters [70].

Symbol	Definition	Value
l_m	Main beam length	0.236 m
l_t	Tail beam length	0.25 m
k_v	Vertical axis friction	0.0095
k_h	Horizontal axis friction	0.0054
J_{mr}	Main propeller inertia	1.65×10^{-5} kgm^2
J_{tr}	Tail propeller inertia	2.65×10^{-5} kgm^2
T_{mr}	Time constant of the main propeller	1.432 s
T_{tr}	Time constant of the tail propeller	0.3842 s
D	Mechanical constant D	1.61×10^{-3}kgm^2
E	Mechanical constant E	4.9×10^{-2} kgm^2
G	Mechanical constant G	6.33×10^{-3}kgm^2
S_f	Balance scale factor	8.43×10^{-4}
g	Gravitational acceleration	9.81 m/s^2

by s_h and s_v, respectively. Table 2 provides a comprehensive description of TRMS parameters. It is crucial to highlight that the actual TRMS was used to validate the model, as described in [70].

The TRMS model described in Eq. (37) corresponds to the MIMO system G shown in Fig. 4, which has two inputs ($p = 2$) and two outputs ($q = 2$). The TRMS output responses are denoted as $y_1(t) = \alpha_h$ for the horizontal axis and $y_2(t) = \alpha_v$ for the vertical axis as shown in Fig. 11. Meanwhile, the control inputs are defined as $u_1(t) = u_h$, corresponding to the main propeller, and the tail propeller is defined as $u_2(t) = u_v$. These inputs correspond to the normalized voltage signals supplied to the individual DC motors. The control inputs $u_1(t)$ and $u_2(t)$ are assigned to the outputs $y_1(t)$ and $y_2(t)$, respectively, in accordance with the physical coupling between the main and tail propellers and their corresponding angular displacements. Due to the strong coupling between the vertical and horizontal dynamics, a centralized control strategy is adopted in the proposed SbLR-BELBIC-PID controller. This formulation allows the control action to be computed from the complete output vector, enabling coordinated control across both axes. In contrast, decentralized approaches that treat each axis independently may fail to capture inter-axis interactions, potentially degrading overall performance. The desired trajectory tracking for both axes is expressed as:

$$\boldsymbol{r}(t) = \begin{bmatrix} r_1(t) & r_2(t) \end{bmatrix}^T. \tag{49}$$

For the purpose of evaluating the SbLR-BELBIC-PID controller, the trajectories are set as follows:

$$r_1(t) = 0.5 \tanh(0.2(t-30)+1)\ radian \tag{50}$$

and

$$r_2(t) = 0.3 \tanh(0.2(t-30))\ radian. \tag{51}$$

Accordingly, the SbLR-BELBIC-PID controller implements the functions $m_{ij}(t)$ and $n_{ij}(t)$ for the SI and RW signals, while $a_{ij}(t)$, $o_{ij}(t)$, and $l_{ij}(t)$ correspond to the amygdala, orbitofrontal cortex, and thalamus nodes, respectively, as described in Section 2. Based on the feedback signals from the system outputs $y_1(t)$ and $y_2(t)$, the controller outputs $u_1(t)$ and $u_2(t)$ were designed without utilizing a decoupling regulator. Therefore, for this configuration, the functions $m_{ij}(t)$, $n_{ij}(t)$, $l_{ij}(t), a_{ij}(t)$, and $o_{ij}(t)$ were set to zero for the pairs $i = 1, j = 2$ and $i = 2, j = 1$. Next, the controller design parameters are arranged in the vector $\boldsymbol{\psi} = [\boldsymbol{K}_P^{SI}, \boldsymbol{K}_I^{SI}, \boldsymbol{K}_D^{SI}, \boldsymbol{N}^{SI}, \boldsymbol{K}_P^{RW}, \boldsymbol{K}_I^{RW}, \boldsymbol{K}_D^{RW}, \boldsymbol{N}^{RW}, \boldsymbol{\varepsilon}, \boldsymbol{\alpha}, \boldsymbol{\beta}, \boldsymbol{\sigma}, \boldsymbol{\gamma}, \boldsymbol{\zeta}, \Delta\boldsymbol{\varepsilon}, \Delta\boldsymbol{\alpha}, \Delta\boldsymbol{\beta}]^T \in \mathbb{R}^{34}$, with dimensionality $n = 34$, as shown in Table 3. The output weights were set as $w_{11} = 1000$ and $w_{12} = 1200$, and the input weights were set as $w_{21} = 1$ and $w_{22} = 1$, with the aim of determining $\boldsymbol{\psi} \in \mathbb{R}^{34}$ in Eq. (22) that minimizes the fitness function $\boldsymbol{J}$. The duration of the simulation was specified as $t_f = 60\ s$. The maximum number of iterations, $k_{max} = 3000$ and the MSEDA coefficients ($K_g = 0.022,\ K_e = 0.75,\ x_{min} = -5.0, x_{max} = 5.0$) were adopted from previous work with the standard BELBIC-PID controller [58]. This ensures a fair control accuracy comparison between the two controllers. A series of preliminary experiments were conducted to determine the initial design parameters, $10^{\boldsymbol{x}(0)} \in \mathbb{R}^{34}$. For instance, some initial design parameters were primarily obtained from our previous work regarding the standard BELBIC-PID controller in our previous work [58]. Meanwhile, the initial design parameters associated with adaptive learning rates were then iteratively fine-tuned to ensure stable output responses. Finally, the setup of all the initial design parameters is summarized in Table 3.

Based on the MSEDA-based technique, Fig. 12 illustrates the convergence curve of the fitness function $\boldsymbol{J}(\boldsymbol{\psi})$ for the proposed SbLR-BELBIC-PID controller over $k_{max} = 3000$ iterations. As detailed in Table 3, the optimal controller design parameters $\boldsymbol{\psi}_{opt}$, based on the MSEDA, effectively minimized the fitness function. Moreover, the output responses of the TRMS horizontal position $y_1(t)$ and vertical position $y_2(t)$ controlled by the SbLR-BELBIC-PID controller are depicted in Figs. 13 and 14, respectively. Correspondingly, Figs. 15 and 16 depict the control input responses $u_1(t)$ and $u_2(t)$, respectively. For performance evaluation, these responses are contrasted with those produced by the standard PID [36], NEPID [36] and the BELBIC-PID controller from our previous work [58]. In Figs. 13–16, the reference is represented by the black line, the PID controller response by the green line, the NEPID controller response by the purple line, the BELBIC-PID controller response by the red line, and the SbLR-BELBIC-PID controller response by the blue line. The findings indicate that the SbLR-BELBIC-PID controller achieved superior trajectory tracking performance compared with the standard PID, NEPID, and BELBIC-PID controllers, as reflected by the lowest value of the fitness function. Moreover, this performance

Table 3
Design parameters for Example 1 (TRMS).

ψ	SbLR-BELBIC-PID gain	$x(0)$	$10^{x(0)}$	x_{opt}	$10^{x_{\text{opt}}}$
ψ_1	$K_{P\ 11}^{SI}$	0.50	3.162	0.633	4.295
ψ_2	$K_{I\ 11}^{SI}$	2.60	398.107	2.260	182.136
ψ_3	$K_{D\ 11}^{SI}$	−0.10	0.794	−0.146	0.715
ψ_4	N_{11}^{SI}	1.60	39.811	1.529	33.765
ψ_5	$K_{P\ 11}^{RW}$	−0.20	0.631	−0.352	0.445
ψ_6	$K_{I\ 11}^{RW}$	2.20	158.489	2.230	169.714
ψ_7	$K_{D\ 11}^{RW}$	0.01	1.023	0.239	1.733
ψ_8	N_{11}^{RW}	2.00	100.000	1.861	72.525
ψ_9	$\varepsilon_{min\ 11}$	−0.30	0.501	−0.413	0.387
ψ_{10}	$\alpha_{min\ 11}$	1.10	12.589	0.880	7.593
ψ_{11}	$\beta_{min\ 11}$	0.00	1.006	0.161	1.447
ψ_{12}	σ_{11}	−1.00	0.100	−0.871	0.135
ψ_{13}	γ_{11}	−0.90	0.126	−1.246	0.057
ψ_{14}	ζ_{11}	−1.05	0.089	−1.076	0.084
ψ_{15}	$\Delta\varepsilon_{11}$	−0.65	0.224	−0.557	0.278
ψ_{16}	$\Delta\alpha_{11}$	−0.80	0.158	−0.622	0.239
ψ_{17}	$\Delta\beta_{11}$	−1.10	0.079	−1.282	0.052
ψ_{18}	$K_{P\ 22}^{SI}$	−2.50	0.003	−2.728	0.002
ψ_{19}	$K_{I\ 22}^{SI}$	−2.20	0.006	−2.389	0.004
ψ_{20}	$K_{D\ 22}^{SI}$	2.30	199.526	2.347	222.520
ψ_{21}	N_{22}^{SI}	4.40	2.51×10^4	4.525	3.35×10^4
ψ_{22}	$K_{P\ 22}^{RW}$	−1.30	0.050	−1.275	0.053
ψ_{23}	$K_{I\ 22}^{RW}$	−1.90	0.013	−1.892	0.013
ψ_{24}	$K_{D\ 22}^{RW}$	2.20	158.489	2.190	154.992
ψ_{25}	N_{22}^{RW}	4.45	2.81×10^4	4.495	3.12×10^4
ψ_{25}	$\varepsilon_{min\ 22}$	0.05	1.122	0.250	1.780
ψ_{27}	$\alpha_{min\ 22}$	0.45	2.818	0.548	3.534
ψ_{28}	$\beta_{min\ 22}$	−1.35	0.045	−1.407	0.039
ψ_{29}	σ_{22}	−1.00	0.100	−1.087	0.082
ψ_{30}	γ_{22}	−1.20	0.063	−1.348	0.045
ψ_{31}	ζ_{22}	−0.90	0.126	−0.887	0.130
ψ_{32}	$\Delta\varepsilon_{22}$	−0.90	0.126	−0.814	0.153
ψ_{33}	$\Delta\alpha_{22}$	−1.20	0.063	−1.418	0.038
ψ_{34}	$\Delta\beta_{22}$	−1.00	0.100	−0.826	0.149

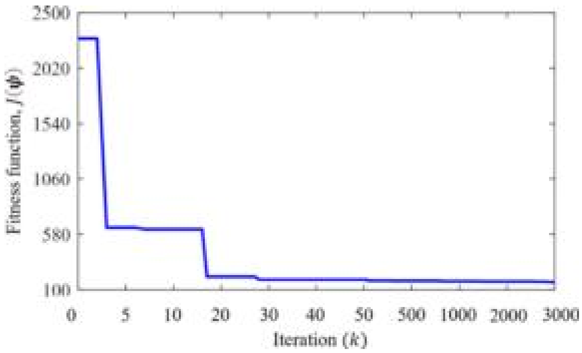

Fig. 12. The fitness function $J(\psi)$, of SbLR-BELBIC-PID for TRMS.

Table 4
Numerical results for Example 1 (TRMS).

Performance Index	PID [36]	NEPID [36]	BELBIC-PID [58]	SbLR-BELBIC-PID
Fitness function $J(\psi)$	306.9743	227.1835	176.2902	**167.0565**
ISE $\sum_{j=1}^{2} \bar{e}_j$	0.2247	0.1536	0.1184	**0.1104**
ISI $\sum_{i=1}^{2} \bar{u}_i$	47.5277	42.3563	44.2307	**43.5869**

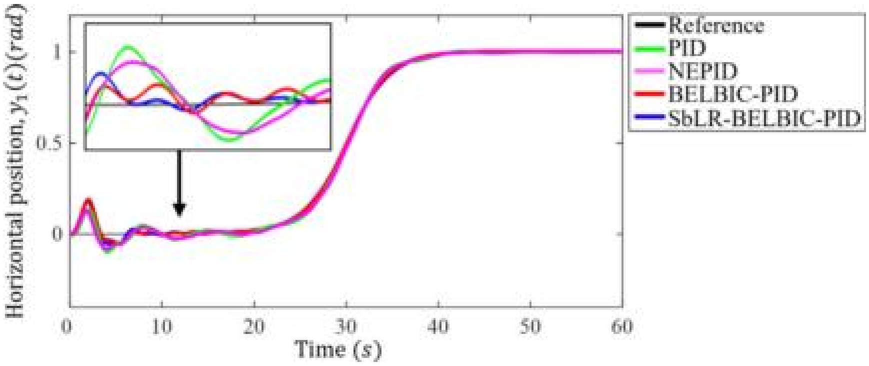

Fig. 13. Horizontal position, $y_1(t)$ responses for all controllers in the TRMS.

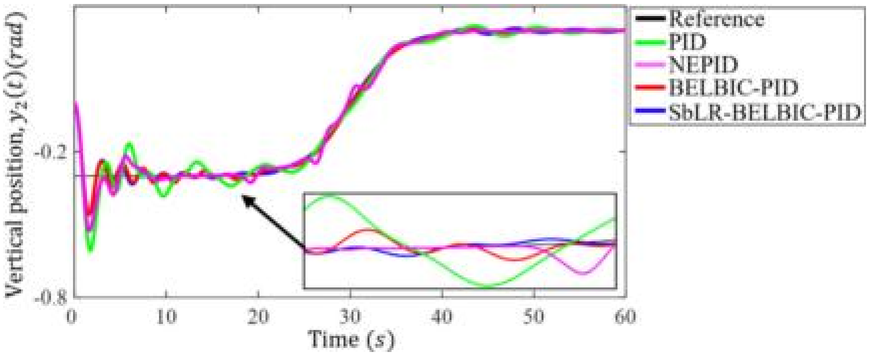

Fig. 14. Vertical position, $y_2(t)$ responses for all controllers in the TRMS.

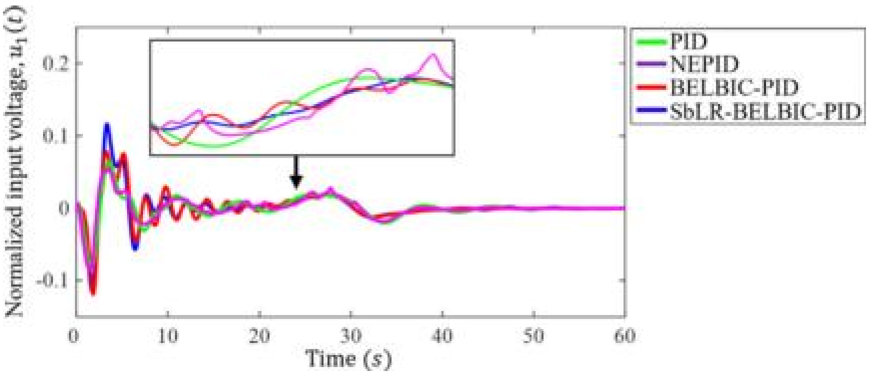

Fig. 15. Normalized input voltage, $u_1(t)$ responses for all controllers in the TRMS.

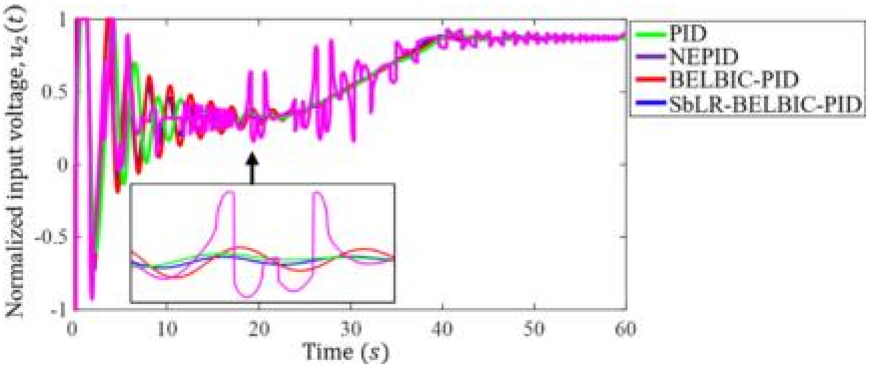

Fig. 16. Normalized input voltage, $u_2(t)$ responses for all controllers in the TRMS.

Table 5
Time response performance results for Example 1 (TRMS).

Response	Performance parameters	PID [36]	NEPID [36]	BELBIC-PID [58]	SbLR-BELBIC-PID
TRMS horizontal position, $y_1(t)$	Settling time (2 %), $T_s(s)$	15.24	12.51	**6.27**	7.30
	Overshoot percentage, $OS(\%)$	13.34	**12.71**	18.91	17.92
TRMS vertical position, $y_2(t)$	Settling time (2 %), $T_s(s)$	55.26	39.48	40.62	**12.37**
	Overshoot percentage, $OS(\%)$	101.93	75.04	52.50	**52.43**

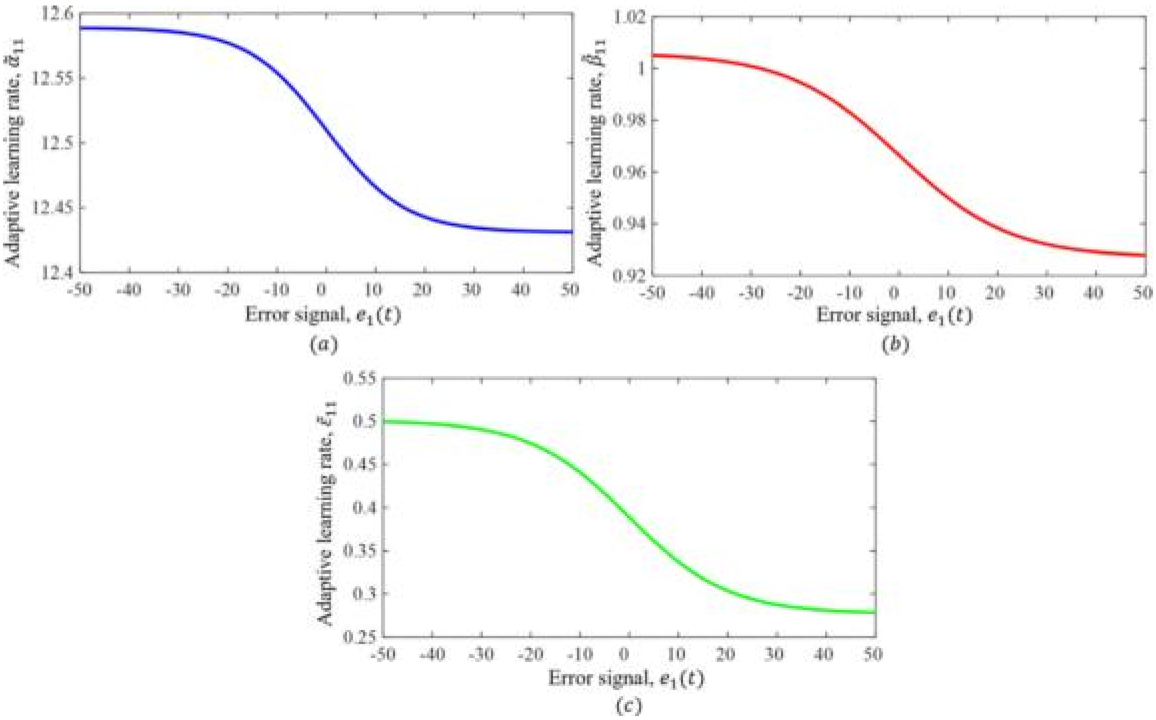

Fig. 17. The sigmoid-based SbLR-BELBIC-PID adaptive learning rates for (a) the amygdala $\tilde{\alpha}_{11}$, (b) the orbitofrontal cortex $\tilde{\beta}_{11}$, and (c) the thalamus $\tilde{\varepsilon}_{11}$ in example 1 (TRMS).

is further substantiated by the lowest ISE and ISI for the SbLR-BELBIC-PID controller, as presented in Table 4. Furthermore, the SbLR-BELBIC-PID controller improved control accuracy, achieving a 5.24 % increase in $J_A(\boldsymbol{\psi})$ relative to the standard BELBIC-PID, as defined in Eq. (32). This underscores the effectiveness of incorporating sigmoid-based emotional learning rates into the standard BELBIC-PID controller. Moreover, this method produces smoother control inputs, $u_1(t)$ and $u_2(t)$, in response to the error signal, as highlighted in the zoomed-in sections of Figs. 15 and 16, resulting in improved control accuracy.

Additionally, the results in Table 5 compare the time response performance of PID, NEPID, BELBIC-PID, and the proposed SbLR-BELBIC-PID controllers for the TRMS's horizontal $y_1(t)$ and vertical $y_2(t)$ positions. The PID controller, serving as a baseline, showed limitations in handling the nonlinear dynamics of the TRMS, particularly for the vertical position $y_2(t)$, where it resulted in a prolonged settling time of 55.26 s and a significant overshoot of 101.93 %. The NEPID controller, as an advanced variant of PID, achieved improved performance with a settling time of 39.48 s and a reduced overshoot of 75.04 %. In contrast, the BELBIC-PID controller demonstrated marked improvements over PID and NEPID, where the settling time was reduced to 6.27 s for $y_1(t)$ and 40.62 s for $y_2(t)$, with overshoots of 18.91 % and 52.50 %, respectively. However, the relatively high overshoot of the BELBIC-PID controller for $y_1(t)$ indicates potential for further enhancement.

Nevertheless, the SbLR-BELBIC-PID controller effectively addressed these shortcomings, achieving a settling time of 7.30 s for $y_1(t)$, reducing the overshoot to 17.92 %. Furthermore, for the vertical position $y_2(t)$, the SbLR-BELBIC-PID controller significantly reduced settling time to 12.37 s, substantially outperforming the BELBIC-PID controller while maintaining a nearly identical overshoot of 75.04 %. These results underscore the effectiveness of the proposed sigmoid-based learning rates in the SbLR-BELBIC-PID controller, particularly in vertical position control. The controller managed to achieve faster reference trajectory tracking while ensuring optimal transient response for complex MIMO systems, such as the TRMS.

Furthermore, the optimal sigmoid-based emotional learning rates for the amygdala ($\tilde{\alpha}_{11}$), orbitofrontal cortex ($\tilde{\beta}_{11}$), and thalamus ($\tilde{\varepsilon}_{11}$) are depicted in Figs. 17(a), (b), and (c), respectively. These functions are associated with the error signal $e_1(t)$, for controlling the horizontal position $y_1(t)$. Similarly, the emotional learning rates $\tilde{\alpha}_{22}$, $\tilde{\beta}_{22}$, and $\tilde{\varepsilon}_{22}$, shown in Figs. 18(a), (b), and (c), respectively,

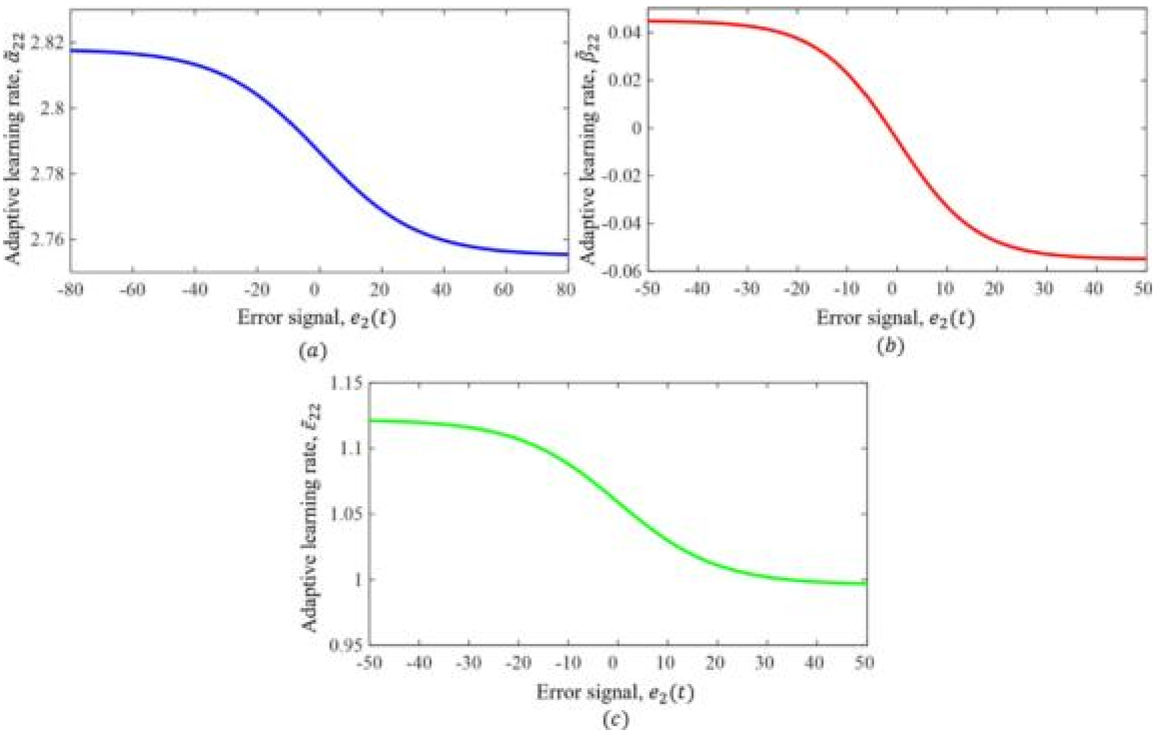

Fig. 18. The sigmoid-based SbLR-BELBIC-PID adaptive learning rates for (a) the amygdala $\tilde{\alpha}_{22}$, (b) the orbitofrontal cortex $\tilde{\beta}_{22}$, and (c) the thalamus $\tilde{\varepsilon}_{22}$ in example 1 (TRMS).

correspond to the emotional learning rates of the same brain regions based on the error signal $e_2(t)$ for controlling the vertical position $y_2(t)$. As shown in Figs. 17 and 18, the magnitude of the emotional learning rates varied with the error signal within specified lower and upper bounds. Once a specific error signal magnitude was reached, the learning rates saturated at the lower or upper bound. This saturation is crucial for preventing undesirable emotional learning responses from excessively low or high learning rates. It must be noted that the emotional learning rates $\tilde{\alpha}_{ij}$, $\tilde{\beta}_{ij}$, and $\tilde{\varepsilon}_{ij}$ (for $i = 1, j = 1$ and $i = 2, j = 2$) were continuously updated in response to the error signals rather than being held constant, as in the standard BELBIC-PID controller described in our previous work [58].

Additionally, the sharpness of transitions at the lower and upper bounds for the amygdala, orbitofrontal cortex, and thalamus enabled flexible control responses that enhanced the brain's emotional learning experience. These transitions yielded optimal emotional learning rates within specified boundaries, determined by the error signals, resulting in faster response times, reduced steady-state error, and improved transient response. Moreover, Figs. 19 and 20 illustrate the time-varying responses of the sigmoid-based emotional learning rates $\tilde{\alpha}_{ij}$, $\tilde{\beta}_{ij}$, and $\tilde{\varepsilon}_{ij}$ for $i = 1, j = 1$ and $i = 2, j = 2$, respectively. These results indicated that the emotional learning rates varied more significantly during the initial 0–15 s for horizontal and vertical position control due to the high error signals present during this transient period. Meanwhile, the variation in emotional learning rates decreased after this period, as the transient error signals significantly diminished and approached a minimal value compared to the initial period. These findings highlight the effectiveness of the sigmoid-based emotional learning rates, which correspond to the error signals, in regulating the output signals of the amygdala, orbitofrontal cortex, and thalamus, as defined in Eqs. (14), (18), and (10), respectively. Thus, this approach enhances control accuracy, demonstrating that the SbLR-BELBIC-PID controller provides superior performance compared with the standard BELBIC-PID [58], NEPID [36] and conventional PID [36] controllers when applied to the TRMS.

5.1.1. Robustness evaluation under measurement noise for TRMS

To further assess the controller performance under realistic operating conditions, a trajectory tracking simulation was conducted by introducing measurement noise $\boldsymbol{e}_{noise}(t)$ into the system. The noise was modeled as zero-mean white noise with a variance of 0.01. As depicted in Fig. 21, the robustness evaluation was configured for the SbLR-BELBIC-PID controller, and the same configuration was adopted for the standard BELBIC-PID to provide an equitable basis for comparison. The optimal control parameters obtained from the noise-free case were applied to ensure consistency. In this setup, the error signal $\boldsymbol{e}(t)$ was obtained by subtracting the measured output signal with noise, $\boldsymbol{y}'(t)$, from the reference signal $\boldsymbol{r}(t)$. The measured noisy output $\boldsymbol{y}'(t)$ was generated by adding the noise signal $\boldsymbol{e}_{noise}(t)$ to the actual plant output, $\boldsymbol{y}(t)$. As shown in Table 6, the proposed SbLR-BELBIC-PID consistently outperformed the BELBIC-PID with lower fitness function, ISE, and ISI values. Furthermore, Table 7 shows that the SbLR-BELBIC-PID also reduced ITAE, ITSE, IAE, and ISE in most cases, particularly for the TRMS horizontal position control, highlighting its improved tolerance to measurement noise. The output responses in Figs. 22 and 23 further illustrate that the proposed controller maintained more stable

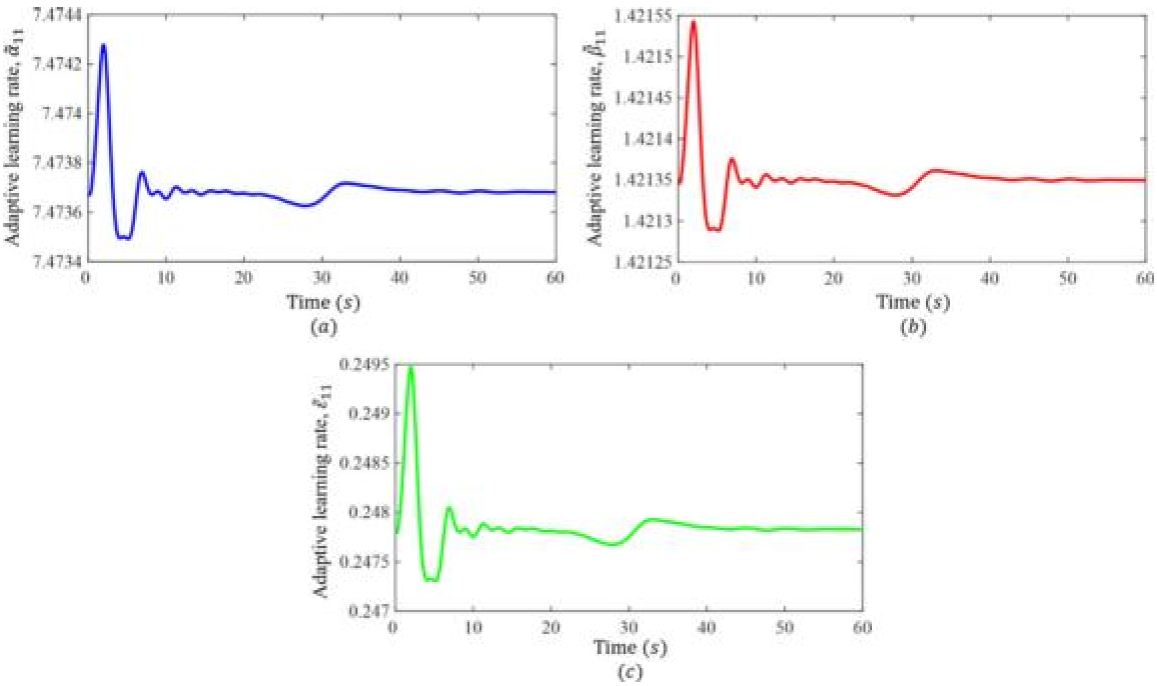

Fig. 19. The SbLR-BELBIC-PID adaptive learning rate responses for (a) the amygdala $\tilde{\alpha}_{11}$, (b) the orbitofrontal cortex $\tilde{\beta}_{11}$, and (c) the thalamus $\tilde{\varepsilon}_{11}$ in example 1 (TRMS).

Table 6
Numerical results under measurement noise for Example 1 (TRMS).

Performance Index	BELBIC-PID [58]	SbLR-BELBIC-PID
Fitness function $J(\boldsymbol{\psi})$	179.3794	**176.7974**
ISE $\sum_{j=1}^{2} \bar{e}_j$	0.1208	**0.1183**
ISI $\sum_{i=1}^{2} \bar{u}_i$	44.7082	**44.2756**

Table 7
Trajectory tracking performance indices under measurement noise for Example 1 (TRMS).

Response	Performance parameters	BELBIC-PID [58]	SbLR-BELBIC-PID
TRMS horizontal position, $y_1(t)$	ITAE	13.1204	**11.5589**
	ITSE	0.2105	**0.1836**
	IAE	0.7927	**0.7462**
	ISE	0.0512	**0.0474**
TRMS vertical position, $y_2(t)$	ITAE	11.6798	**11.6387**
	ITSE	**0.1670**	0.1824
	IAE	**0.8551**	0.8637
	ISE	**0.0696**	0.0709

tracking performance under noisy measurements for both horizontal and vertical positions. Moreover, it required lower control input energy compared to the standard BELBIC-PID as shown in Figs. 24 and 25. These findings confirm that the proposed adaptive learning rate, which adjusts in response to the magnitude of error signals, enhances the emotional learning process and leads to improved control accuracy and robustness.

5.2. Example 2: container gantry crane system

Fig. 26 illustrates the operation of a container gantry crane system, where the crane payload undergoes swinging motion due to the movement of the trolley. Notably, this study adopted the model and confirmed its validity through the experimental rig of the

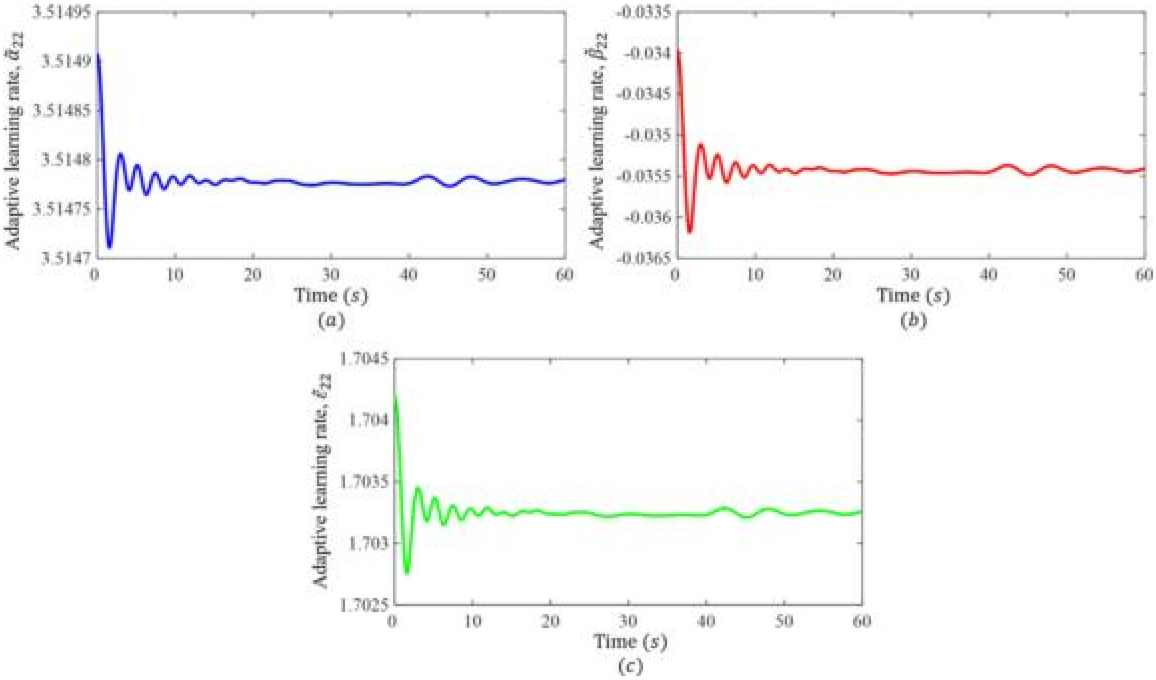

Fig. 20. The SbLR-BELBIC-PID adaptive learning rate responses for (a) the amygdala $\tilde{\alpha}_{22}$, (b) the orbitofrontal cortex $\tilde{\beta}_{22}$, and (c) the thalamus $\tilde{\varepsilon}_{22}$ in example 1 (TRMS).

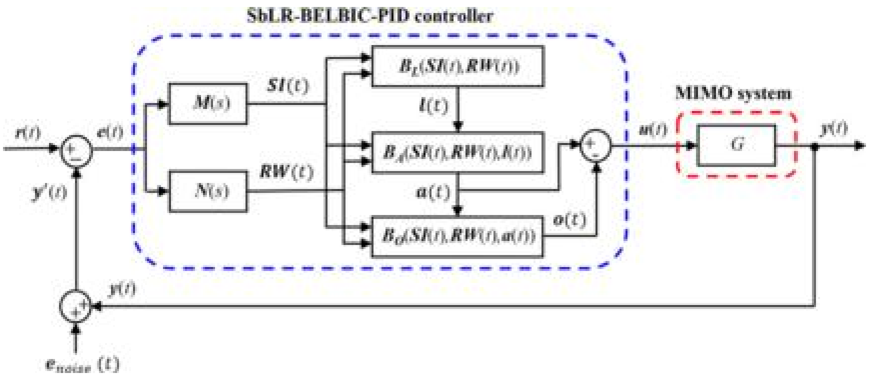

Fig. 21. TRMS system in the presence of measurement noise.

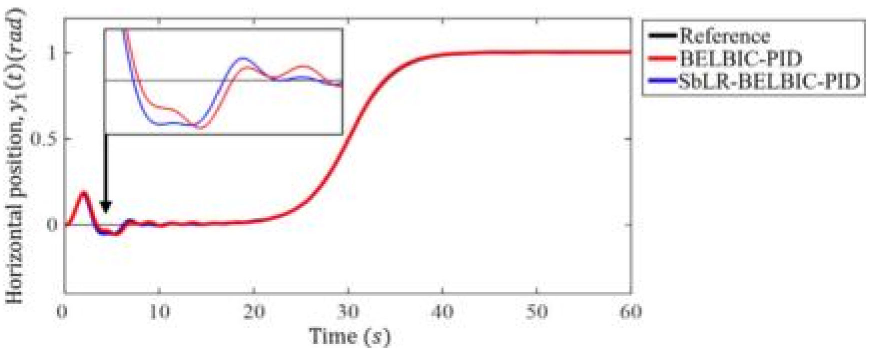

Fig. 22. TRMS horizontal position, $y_1(t)$ responses under measurement noise.

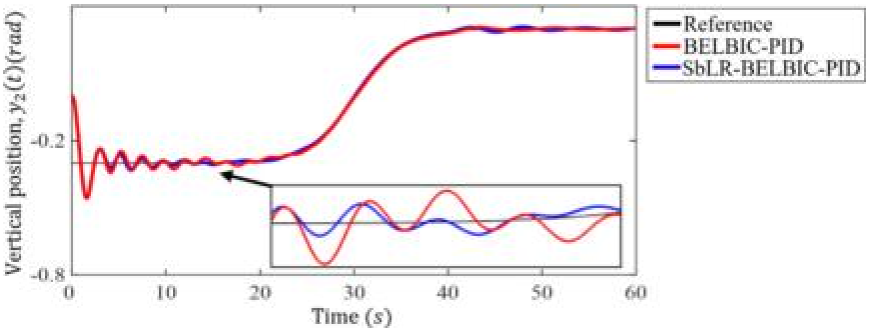

Fig. 23. TRMS vertical position, $y_2(t)$ responses under measurement noise.

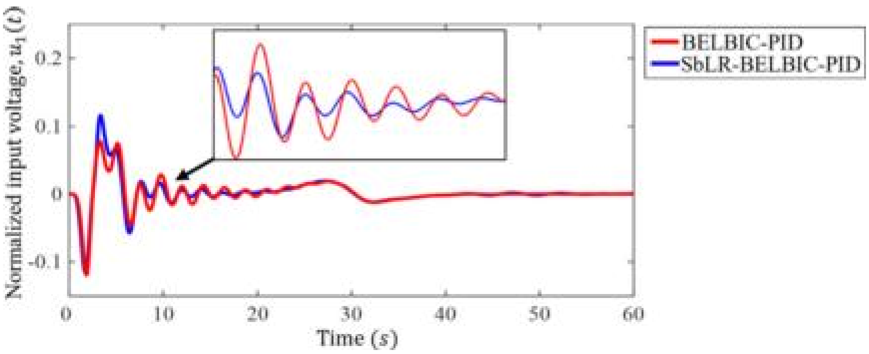

Fig. 24. TRMS normalized input voltage, $u_1(t)$ responses under measurement noise.

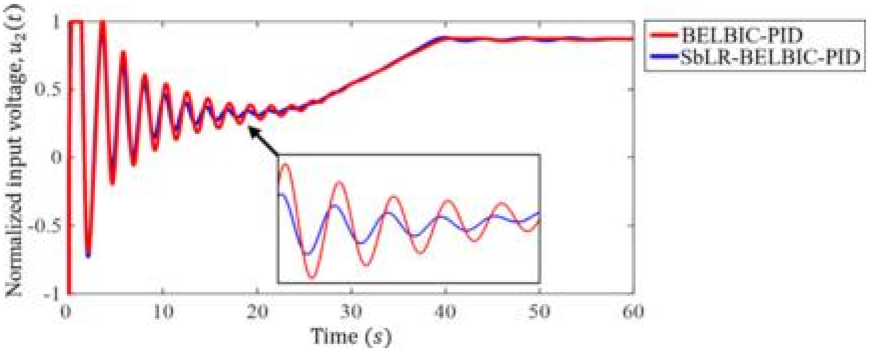

Fig. 25. TRMS normalized input voltage, $u_2(t)$ responses under measurement noise.

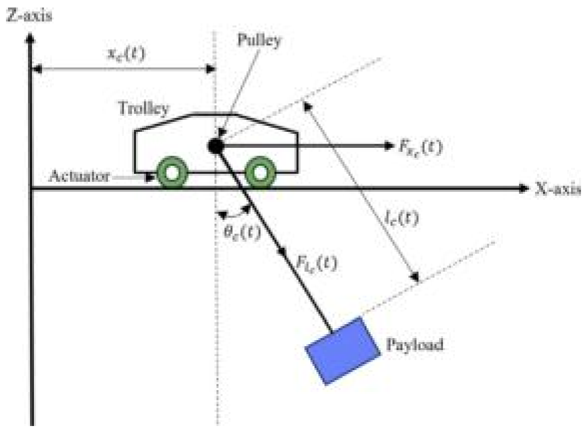

Fig. 26. The gantry crane system.

gantry crane system [71,72]. The X and Z-axes represent the trolley's horizontal and vertical paths. The system outputs are defined as $x_c(t)$ for the trolley displacement, $l_c(t)$ for the payload rope length, and $\theta_c(t)$ for the payload sway angle. The control input $F_{x_c}(t)$ governs the trolley's horizontal motion while $F_{l_c}(t)$ controls the hoist movement along the l_c-direction. The dynamic model of the gantry crane system, known as system G in Fig. 4, was expressed through the following equations:

$$\boldsymbol{x}_a = \begin{bmatrix} \boldsymbol{q} \\ -\boldsymbol{D}^{-1}(\boldsymbol{q})[\boldsymbol{W}_{\boldsymbol{m}}(\boldsymbol{q},\boldsymbol{q})\,\boldsymbol{q}+\boldsymbol{R}(\boldsymbol{q})\end{bmatrix} - \begin{bmatrix} 0_{3\times3} \\ -\boldsymbol{D}^{-1}(\boldsymbol{q})\end{bmatrix}\begin{bmatrix}1 & 0 & 0\\ 0 & 1 & 0\end{bmatrix}^T \boldsymbol{u}, \tag{52}$$

where $\boldsymbol{x}_a = [x_c\ l_c\ \theta_c\ \ x_c\ \ l_c\ \ \theta_c]^T$, $\boldsymbol{u} = [\ u_1 \quad u_2\ ]^T = [\ F_{x_c} \quad F_{l_c}\ ]^T$, $\boldsymbol{q} = [x_c\ l_c\ \theta_c]^T$,

$$\boldsymbol{D}(\boldsymbol{q}) = \begin{bmatrix} m_p + m_t & m_p \sin\theta_c & m_p l_c \cos\theta_c \\ m_p \sin\theta_c & m_p + m_l & 0 \\ m_p l_c \cos\theta_c & 0 & m_p l_c{}^2 + I \end{bmatrix}, \tag{53}$$

$$\boldsymbol{W}_{\boldsymbol{m}}(\boldsymbol{q},\boldsymbol{q}) = \begin{bmatrix} 0 & m_p\,\theta_c \cos\theta_c & -m_p l_c \sin\theta_c\,\theta_c + m_p \cos\theta_c\, l_c \\ 0 & 0 & -m_p l_c\,\theta_c \\ 0 & m_p l_c\,\theta_c & m_p l_c\, l_c \end{bmatrix}, \tag{54}$$

and

$$\boldsymbol{R}(\boldsymbol{q}) = [\ 0 \quad -m_p g \cos\theta_c \quad m_p g l_c \sin\theta_c\ ]^T. \tag{55}$$

Subsequently, the output vector of the gantry crane system is expressed as:

$$\boldsymbol{y} = \begin{bmatrix} 1 & 0 & 0\,0 & 0 & 0 \\ 0 & 1 & 0\,0 & 0 & 0 \\ 0 & 0 & 1\,0 & 0 & 0 \end{bmatrix}\begin{bmatrix} x_c \\ l_c \\ \theta_c \\ x_c \\ l_c \\ \theta_c \end{bmatrix} = \begin{bmatrix} x_c \\ l_c \\ \theta_c \end{bmatrix} = \boldsymbol{q}. \tag{56}$$

The proposed SbLR-BELBIC-PID controller adopts a centralized configuration, consistent with the approach discussed in Section 5.1. Based on Eqs. (53)–(55), the essential parameters of the gantry crane system are defined as follows: the payload mass $m_p = 0.73$ kg, trolley mass $m_t = 1.06$ kg, rope mass $m_l = 0.5$ kg, and moment of inertia $I = 0.005\ \mathrm{kgm}^2$. These values were adopted from a previous study [58].

As shown in Fig. 4, the SbLR-BELBIC-PID controller was employed to control the MIMO gantry crane system. A system with $p = 2$ inputs and $q = 3$ outputs is illustrated in Fig. 26. The inputs of the system are represented by $u_1(t) = F_{x_c}(t)$ and $u_2(t) = F_{l_c}(t)$, which correspond to the trolley force and hoist force, respectively. The corresponding outputs are the trolley displacement $y_1(t) = x_c(t)$, payload rope length $y_2(t) = l_c(t)$, and payload sway angle $y_3(t) = \theta_c(t)$. The control objectives are specified as:

$$\boldsymbol{r}(t) = [\ 0 \quad 0.2 \quad 0\ ]^T\ \forall\, t, \tag{57}$$

with initial output conditions $x_c(0) = 1$, $l_c(0) = 1$, and $\theta_c(0) = 0$. Furthermore, the SbLR-BELBIC-PID controller described in Section 2 was implemented based on the functions $m_{ij}(t)$, $n_{ij}(t)$, $a_{ij}(t)$, $o_{ij}(t)$, and $l_{ij}(t)$. The controller was designed to position the crane payload at the desired position while minimizing the sway angle. Therefore, given the underactuated nature of the gantry crane system, the control input $u_1(t)$ was determined from feedback signals of $y_1(t)$ and $y_3(t)$, while the feedback signal of $y_2(t)$ solely determined $u_2(t)$. Consequently, the controller functions were then set as $m_{ij}(t) = 0$, $n_{ij}(t) = 0$, $l_{ij}(t) = 0$, $a_{ij}(t) = 0$, $o_{ij}(t) = 0$ when $i = 1$ and $j = 2$, and similarly when $i = 2$ and $j \in \{1, 3\}$. Following this setup, the design parameters were defined with a dimension of $n = 51$, and expressed as $\boldsymbol{\psi} = [\boldsymbol{K}_{\boldsymbol{P}}^{\boldsymbol{SI}}, \boldsymbol{K}_{\boldsymbol{I}}^{\boldsymbol{SI}}, \boldsymbol{K}_{\boldsymbol{D}}^{\boldsymbol{SI}}, \boldsymbol{N}^{\boldsymbol{SI}}, \boldsymbol{K}_{\boldsymbol{P}}^{\boldsymbol{RW}}, \boldsymbol{K}_{\boldsymbol{I}}^{\boldsymbol{RW}}, \boldsymbol{K}_{\boldsymbol{D}}^{\boldsymbol{RW}}, \boldsymbol{N}^{\boldsymbol{RW}}, \boldsymbol{\varepsilon}, \boldsymbol{\alpha}, \boldsymbol{\beta}, \boldsymbol{\sigma}, \boldsymbol{\gamma}, \boldsymbol{\zeta}, \Delta\boldsymbol{\varepsilon}, \Delta\boldsymbol{\alpha}, \Delta\boldsymbol{\beta}]^T \in \mathbb{R}^{51}$, as listed in Table 8. The output weights were set as $w_{11} = 200$, $w_{12} = 400$, and $w_{13} = 200$, while the input weights were set as $w_{21} = 1$ and $w_{22} = 1$ to determine $\boldsymbol{\psi} \in \mathbb{R}^{51}$ in Eq. (22), which minimizes the fitness function J. Additionally, the simulation was conducted with a specific duration of $t_f = 20\ s$. For all design parameters, the search space was bounded by a lower limit of $x_{min} = -5.0$ and an upper limit of $x_{max} = 5.0$. Moreover, the maximum number of iterations was set to $k_{max} = 3000$, and the MSEDA coefficients $K_g = 0.022$ and $K_e = 0.75$ were taken from prior work with the standard BELBIC-PID controller [58], ensuring a fair comparison in control accuracy between the two controllers. To determine the initial design parameters $10^{\boldsymbol{x}(0)} \in \mathbb{R}^{51}$, a series of preliminary experiments were conducted following the same methodology as in Example 1. The final setup of all initial design parameters is summarized in Table 8.

Subsequently, Fig. 27 shows the convergence curve of the fitness function $J(\boldsymbol{\psi})$, which was optimized using the MSEDA-based technique over $k_{max} = 3000$ iterations. As shown in Fig. 27, the fitness function approached its saturation value at approximately $k > 2000$ iterations, reflecting the complexity of tuning the proposed SbLR-BELBIC-PID controller with 51 design parameters using MSEDA for the gantry crane system. Consequently, these results demonstrated that the MSEDA-based technique successfully minimized the fitness function, yielding the optimal control design parameters $\boldsymbol{\psi}_{opt}$, as listed in Table 8, despite the larger number of design parameters. Furthermore, the system output responses $y_1(t)$, $y_2(t)$, and $y_3(t)$ are illustrated in Figs. 28, 29, and 30, respectively. Similarly, the corresponding control input of the trolley force $u_1(t)$ and hoist force $u_2(t)$ responses are shown in Figs. 31 and 32, respectively. For comparison, the performance of the proposed SbLR-BELBIC-PID controller was assessed alongside the standard

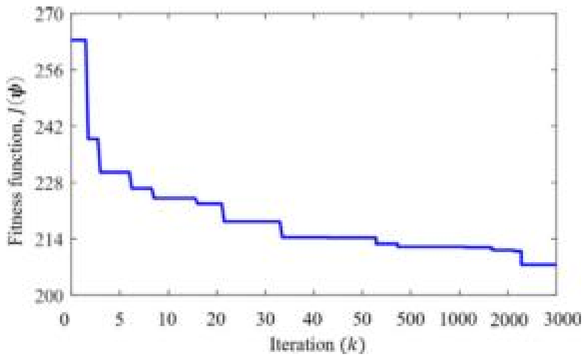

Fig. 27. Convergence curve of the fitness function $J(\boldsymbol{\psi})$ for the SbLR-BELBIC-PID controller applied to the gantry crane system.

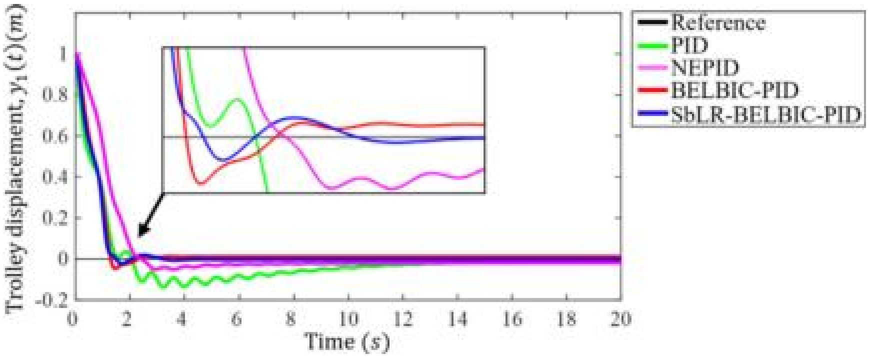

Fig. 28. The gantry crane trolley displacement, $y_1(t)$ responses.

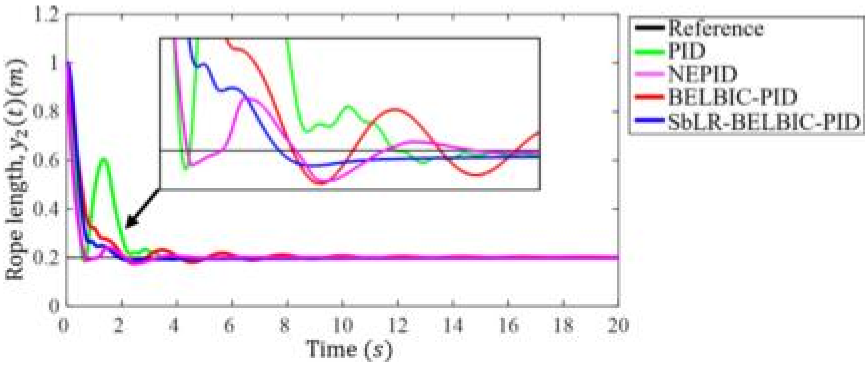

Fig. 29. The gantry crane rope length, $y_2(t)$ responses.

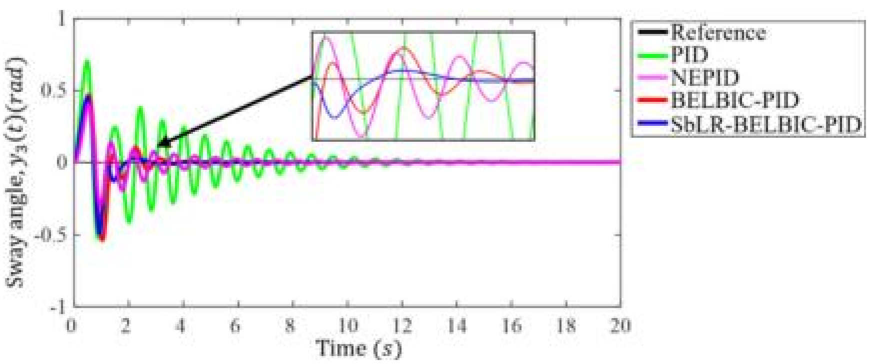

Fig. 30. The gantry crane payload sway angle, $y_3(t)$ responses.

Table 8
Design parameters for Example 2 (Gantry crane system).

ψ	SbLR-BELBIC-PID gain	$x(0)$	$10^{x(0)}$	x_{opt}	$10^{x_{opt}}$
ψ_1	$K^{SI}_{P\ 11}$	−0.70	0.200	−0.652	0.223
ψ_2	$K^{SI}_{I\ 11}$	2.50	316.228	2.522	332.382
ψ_3	$K^{SI}_{D\ 11}$	−0.10	0.794	−0.117	0.764
ψ_4	N^{SI}_{11}	1.50	31.623	1.431	26.992
ψ_5	$K^{RW}_{P\ 11}$	−0.20	0.631	−0.567	0.271
ψ_6	$K^{RW}_{I\ 11}$	2.40	251.189	2.475	298.838
ψ_7	$K^{RW}_{D\ 11}$	1.70	50.119	2.213	163.380
ψ_8	N^{RW}_{11}	2.00	100.000	2.018	104.174
ψ_9	$\epsilon_{min\ 11}$	−0.10	0.794	−0.012	0.973
ψ_{10}	$\alpha_{min\ 11}$	2.50	316.228	2.344	220.531
ψ_{11}	$\beta_{min\ 11}$	0.50	3.162	0.446	2.793
ψ_{12}	σ_{11}	−0.05	0.891	0.436	2.729
ψ_{13}	γ_{11}	0.70	5.012	0.635	4.311
ψ_{14}	ζ_{11}	1.00	10.000	0.708	5.102
ψ_{15}	$\Delta\epsilon_{11}$	0.75	5.623	0.848	7.043
ψ_{16}	$\Delta\alpha_{11}$	2.20	158.489	2.340	218.561
ψ_{17}	$\Delta\beta_{11}$	1.60	39.811	1.642	43.844
ψ_{18}	$K^{SI}_{P\ 13}$	−0.80	0.159	−1.061	0.087
ψ_{19}	$K^{SI}_{I\ 13}$	1.20	15.849	1.338	21.775
ψ_{20}	$K^{SI}_{D\ 13}$	0.70	5.012	0.356	2.270
ψ_{21}	N^{SI}_{13}	1.00	10.000	1.312	20.526
ψ_{22}	$K^{RW}_{P\ 13}$	−1.00	0.100	−0.739	0.182
ψ_{23}	$K^{RW}_{I\ 13}$	1.00	10.000	1.280	19.072
ψ_{24}	$K^{RW}_{D\ 13}$	−0.10	0.794	−0.419	0.381
ψ_{25}	N^{RW}_{13}	1.60	39.811	1.754	56.725
ψ_{26}	$\epsilon_{min\ 13}$	0.90	7.943	1.183	15.254
ψ_{27}	$\alpha_{min\ 13}$	1.30	19.953	1.287	19.349
ψ_{28}	$\beta_{min\ 13}$	−0.40	0.398	−0.651	0.224
ψ_{29}	σ_{13}	0.30	1.995	0.416	2.609
ψ_{30}	γ_{13}	0.70	5.012	0.915	8.231
ψ_{31}	ζ_{13}	−0.40	0.398	0.014	1.033
ψ_{32}	$\Delta\epsilon_{13}$	1.00	10.000	1.265	18.421
ψ_{33}	$\Delta\alpha_{13}$	1.50	31.623	1.442	27.692
ψ_{34}	$\Delta\beta_{13}$	1.35	22.387	1.698	49.864
ψ_{35}	$K^{SI}_{P\ 22}$	2.00	100.000	1.947	88.470
ψ_{36}	$K^{SI}_{I\ 22}$	−0.10	0.794	−0.029	0.935
ψ_{37}	$K^{SI}_{D\ 22}$	−0.40	0.398	−0.524	0.299
ψ_{38}	N^{SI}_{22}	0.50	3.162	0.570	3.714
ψ_{39}	$K^{RW}_{P\ 22}$	1.70	50.119	1.675	47.313
ψ_{40}	$K^{RW}_{I\ 22}$	0.50	3.162	0.352	2.251
ψ_{41}	$K^{RW}_{D\ 22}$	−1.30	0.050	−1.852	0.014
ψ_{42}	N^{RW}_{22}	0.85	7.080	0.241	1.741
ψ_{43}	$\epsilon_{min\ 22}$	−1.30	0.050	−0.798	0.159
ψ_{44}	$\alpha_{min\ 22}$	−2.20	0.006	−2.189	0.007
ψ_{45}	$\beta_{min\ 22}$	−4.05	8.91×10^{-5}	−3.767	1.71×10^{-4}
ψ_{46}	σ_{22}	0.80	6.310	0.567	3.686
ψ_{47}	γ_{22}	1.10	12.589	0.483	3.037
ψ_{48}	ζ_{22}	0.30	1.995	0.360	2.292
ψ_{49}	$\Delta\epsilon_{22}$	2.80	630.957	2.211	162.416
ψ_{50}	$\Delta\alpha_{22}$	2.60	398.107	2.726	532.636
ψ_{51}	$\Delta\beta_{22}$	−4.00	1.00×10^{-4}	−3.676	2.11×10^{-4}

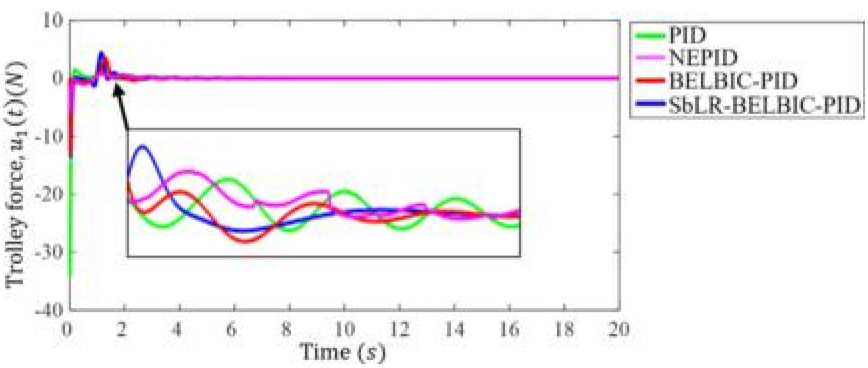

Fig. 31. The gantry crane trolley force, $u_1(t)$ responses.

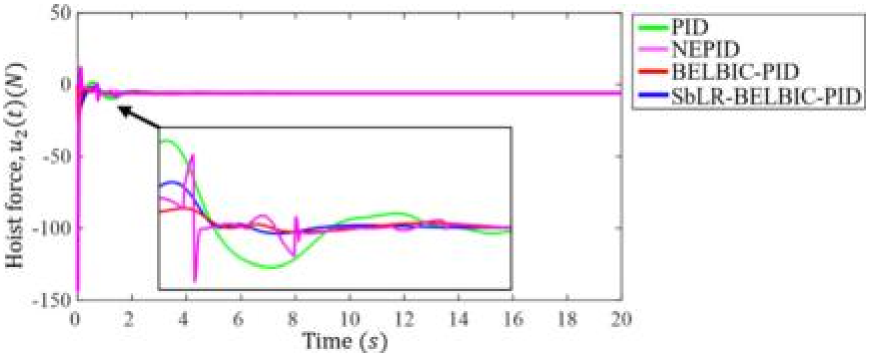

Fig. 32. The gantry crane hoist force, $u_2(t)$ responses.

Table 9
Numerical results for Example 2 (Gantry crane system).

Performance Index	PID [36]	NEPID [36]	BELBIC-PID [58]	SbLR-BELBIC-PID
Fitness function J	333.1457	209.8371	225.1857	**207.5840**
ISE $\sum_{j=1}^{3} \bar{e}_j$	1.0775	0.7189	0.7939	**0.7155**
ISI $\sum_{i=1}^{2} \bar{u}_i$	70.1729	30.1164	27.9262	**26.9831**

Table 10
Time response performance results for Example 2 (Gantry crane system).

Response	Performance parameters	PID [36]	NEPID [36]	BELBIC-PID [58]	SbLR-BELBIC-PID
Trolley displacement, $y_1(t)$	Rise time, $T_r(s)$	1.29	1.90	1.18	**1.12**
	Settling time (2 %), $T_s(s)$	13.53	11.43	1.99	**1.80**
	Overshoot percentage, $OS(\%)$	13.76	5.00	4.59	**2.27**
Rope length, $y_2(t)$	Rise time, $T_r(s)$	**0.49**	0.51	1.25	0.71
	Settling time (2 %),$T_s(s)$	3.27	1.93	5.81	**1.71**
	Overshoot percentage,$OS(\%)$	40.53	2.91	3.16	**1.16**
Payload sway angle, $y_3(t)$	Settling time (2 %), $T_s(s)$	10.72	6.34	3.26	**2.50**
	Maximum sway angle (rad)	0.70	**0.40**	0.47	0.44

PID [36], the NEPID [36] and the standard BELBIC-PID controller from our previous work [58]. Here, the proposed SbLR-BELBIC-PID controller demonstrated superior trajectory tracking performance, as indicated by its lowest fitness function value. As shown in Table 9, this is further supported by the SbLR-BELBIC-PID controller achieving the lowest values for the ISE and the ISI. Moreover, the control accuracy improvement, $J_A(\boldsymbol{\psi})$, defined in Eq. (32), was 7.82 % for the SbLR-BELBIC-PID over the standard BELBIC-PID. This underscores the effectiveness of integrating sigmoid-based emotional learning rates, which also contribute to smoother control input responses, as highlighted in the zoomed-in regions of $u_1(t)$ and $u_2(t)$ in Figs. 31 and 32, thereby further enhancing overall control accuracy.

Furthermore, the time response performance results of the proposed SbLR-BELBIC-PID controller, compared to the PID [36], the NEPID [36] and standard BELBIC-PID [58] controllers, for the gantry crane system are shown in Table 10. For trolley displacement, the PID controller, serving as the baseline benchmark, demonstrated a rise time of 1.29 s, a settling time of 13.53 s, and an overshoot of 13.76 %. Its advanced variant, the NEPID, improved performance by reducing the settling time to 11.43 s and the overshoot to 5.00 %, although the rise time was comparable at 1.90 s. In contrast, the BELBIC-PID controller enhanced performance, reducing the settling time to 1.99 s and the overshoot to 4.59 %, with a rise time of 1.18 s. The SbLR-BELBIC-PID controller improved control accuracy, reducing the settling time to 1.80 s and the overshoot to just 2.27 %, demonstrating superior control over the standard BELBIC-PID controller. Similarly, although the PID controller exhibited a fast rise time of 0.49 s for rope length, its significant overshoot of 40.53 % and settling time of 3.27 s limited its overall control performance.

In contrast, the BELBIC-PID controller improved these metrics by reducing the overshoot to 3.16 % and settling time to 5.81 s. Once again, the proposed controller outperformed the standard BELBIC-PID by achieving the shortest settling time of 1.71 s, the lowest overshoot of 1.16 %, and a faster rise time of 0.71 s. For the payload sway angle, the PID controller resulted in a maximum sway angle of 0.70 rad with a settling time of 10.72 s, while the NEPID controller improved these values to 0.40 rad and 6.34 s, respectively. Conversely, the BELBIC-PID controller achieved a slightly higher sway angle of 0.47 rad compared to NEPID, but it improved the settling time considerably to 3.26 s. Furthermore, the SbLR-BELBIC-PID controller delivered the best performance, with the fastest settling time of 2.50 s and a lower maximum sway angle of 0.44 rad. Overall, the proposed SbLR-BELBIC-PID controller demonstrated superior performance over the standard BELBIC-PID in controlling the gantry crane system. It reduced settling times

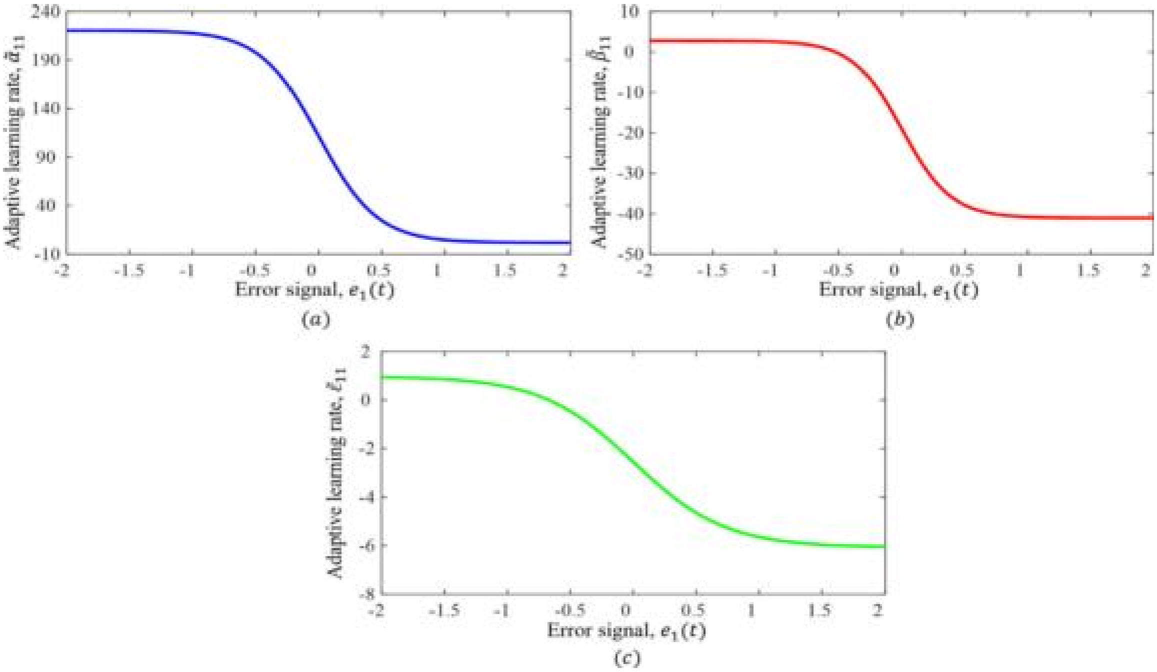

Fig. 33. The sigmoid-based SbLR-BELBIC-PID adaptive learning rates for (a) the amygdala $\tilde{\alpha}_{11}$, (b) the orbitofrontal cortex $\tilde{\beta}_{11}$, and (c) the thalamus $\tilde{\varepsilon}_{11}$ in example 2 (Gantry crane system).

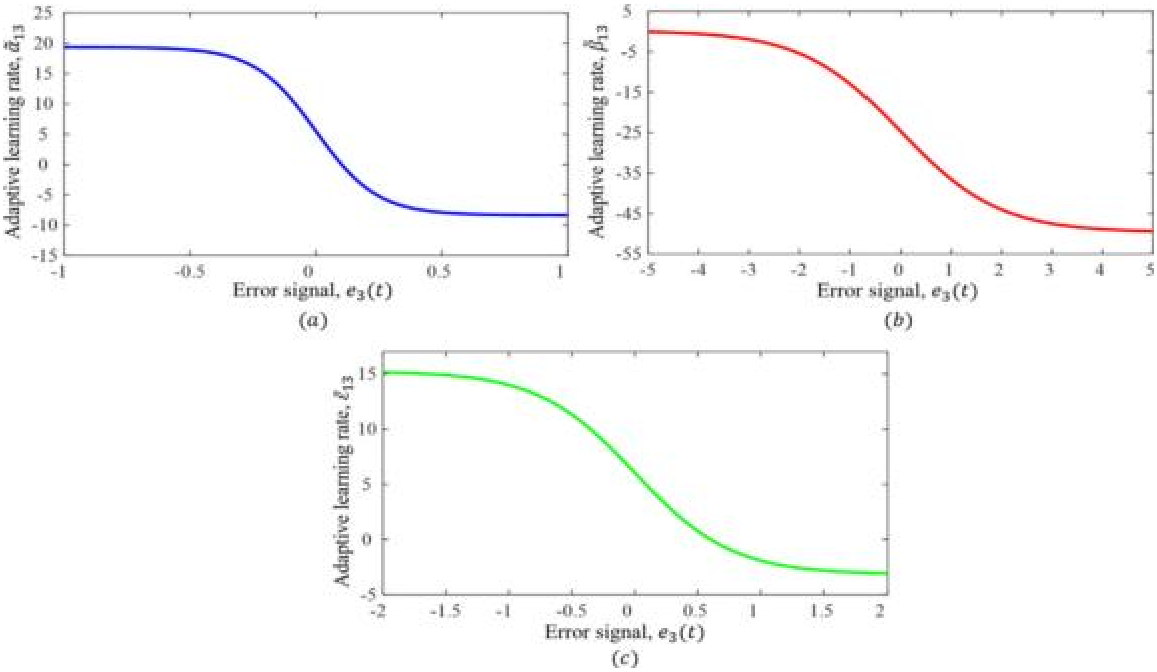

Fig. 34. The sigmoid-based SbLR-BELBIC-PID adaptive learning rates for (a) the amygdala $\tilde{\alpha}_{13}$, (b) the orbitofrontal cortex $\tilde{\beta}_{13}$, and (c) the thalamus $\tilde{\varepsilon}_{13}$ in example 2 (Gantry crane system).

and overshoots while improving transient response, demonstrating the significant impact of sigmoid-based emotional learning rates on enhancing control accuracy.

Furthermore, Figs. 33 and 34 illustrate the sigmoid-based adaptive learning rate behavior for $i = 1$, $j = 1$, and $i = 1$, $j = 3$ of the BELBIC-PID controller, corresponding to the error signals $e_1(t)$ and $e_3(t)$, respectively. Similarly, Fig. 35 depicts the controller's adaptive learning rate adjustment for $i = 2$, $j = 2$, corresponding to the error signal $e_2(t)$. As illustrated in Figs. 33–35, the magnitude of the emotional learning rates varied in response to the error signals, constrained within specified lower and upper bounds. Once the

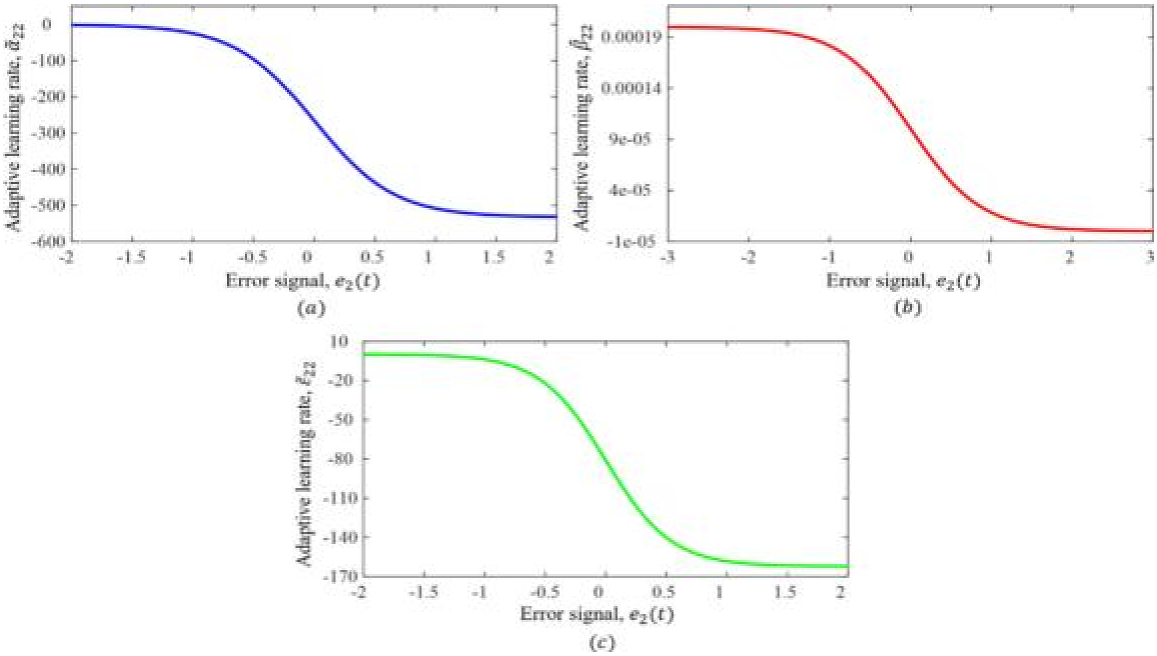

Fig. 35. The sigmoid-based SbLR-BELBIC-PID adaptive learning rates for (a) the amygdala $\tilde{\alpha}_{22}$, (b) the orbitofrontal cortex $\tilde{\beta}_{22}$, and (c) the thalamus $\tilde{\varepsilon}_{22}$ in example 2 (Gantry crane system).

error signal reached a predefined threshold, the learning rates saturated at the lower or upper bound. This saturation mechanism is critical for preventing undesirable emotional learning behaviors in the mammalian brain due to excessively low or high learning rates. Note that the magnitudes of the lower and upper bounds of the learning rates differed for the thalamus, amygdala, and orbitofrontal cortex. This variation in the magnitude of the learning rate reflects changes in response sensitivities, thereby enabling more adaptive responses based on the error signal. Moreover, the emotional learning rates $\tilde{\alpha}_{ij}$, $\tilde{\beta}_{ij}$, and $\tilde{\varepsilon}_{ij}$ were continuously updated in response to the error signals, specifically for $i = 1$ with $j \in \{1, 3\}$, and for $i = 2$ with $j = 2$, distinguishing them from the fixed learning rates in the standard BELBIC-PID controller [58].

Additionally, the adaptive learning rate patterns in the thalamus, amygdala, and orbitofrontal cortex demonstrated consistent behavior, highlighting the importance of the learning rates corresponding to the error signal magnitude in providing appropriate output responses. This leads to faster response times, reduced overshoot, and improved transient response compared to the standard BELBIC-PID, as shown in Table 10. Moreover, Figs. 36 and 37 present the time-varying responses of the sigmoid-based emotional learning rates $\tilde{\alpha}_{ij}$, $\tilde{\beta}_{ij}$, and $\tilde{\varepsilon}_{ij}$ for $i = 1$, $j = 1$, and $i = 1$, $j = 3$, respectively. The results demonstrated that the adaptive learning rates exhibited more significant variation during the initial 0–4 s for gantry crane displacement position and rope length control, corresponding to the high error signals during this transient period. Subsequently, the variation in the emotional learning rates diminished as the transient error signals decreased and approached minimal values compared to the initial period. Additionally, the sigmoid-based emotional learning rates $\tilde{\alpha}_{ij}$, $\tilde{\beta}_{ij}$, and $\tilde{\varepsilon}_{ij}$ for $i = 2$ and $j = 2$ as shown in Fig. 38, exhibited more substantial variation during the first 0–2 s for gantry crane payload sway angle control, corresponding to the elevated error signals during this period. These findings highlight the effectiveness of the sigmoid-based emotional learning rates in adjusting the amygdala, orbitofrontal cortex, and thalamus output signals corresponding to the error signals. Therefore, this mechanism enhances the control accuracy of the controller, justifying that the proposed SbLR-BELBIC-PID controller outperforms the benchmark controllers in terms of control performance for the gantry crane system.

5.2.1. Robustness evaluation under measurement noise for gantry crane system

The robustness evaluation for the gantry crane system was conducted using the same noise characteristics and simulation configuration described in Section 5.1.1. The same optimal control parameters obtained from the noise-free case were applied to ensure a fair and consistent comparison. As presented in Table 11, the proposed SbLR-BELBIC-PID achieved superior performance compared to the standard BELBIC-PID, exhibiting lower values in the fitness function, ISE, and ISI across all evaluated indices. Moreover, the results in Table 12 further highlights that all trajectory tracking indices (ITAE, ITSE, IAE, and ISE) showed improved performance for each output response of the gantry crane system. Additionally, the output responses in Figs. 39–41 illustrate that the SbLR-BELBIC-PID maintained accurate trolley displacement tracking, precise rope length control, and effectively reduced payload oscillations under noisy measurement conditions. Furthermore, the adaptive learning rate mechanism enabled more responsive control actions according to the magnitude of the error signals, as illustrated in Figs. 42 and 43, thereby sustaining superior control performance with improved efficiency.

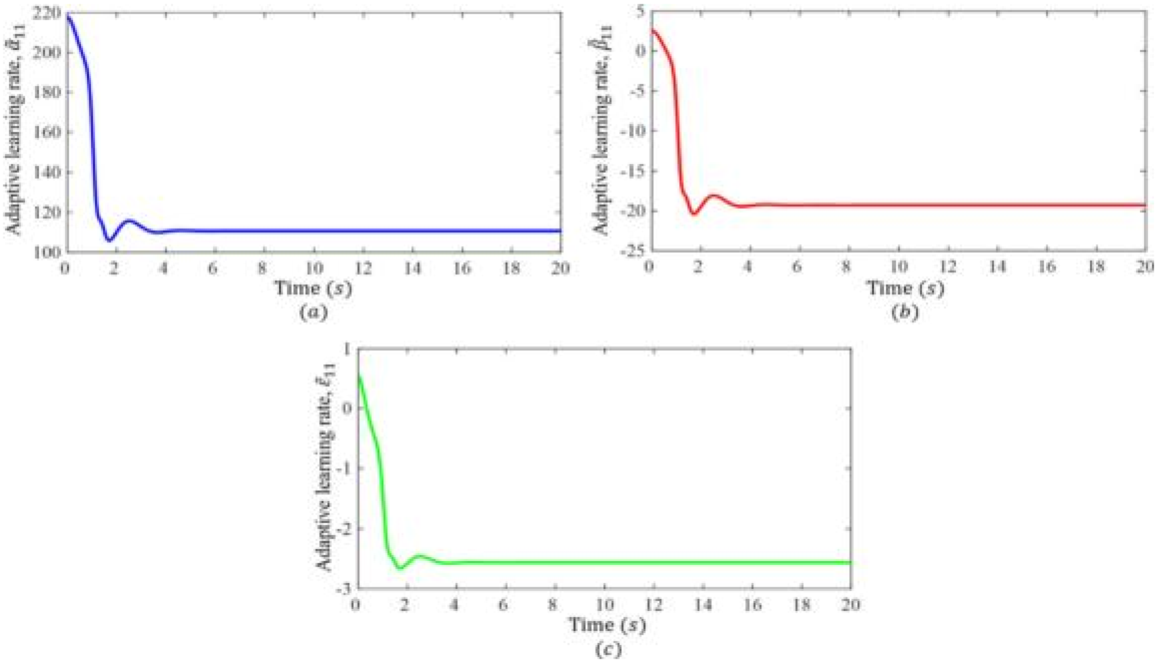

Fig. 36. The SbLR-BELBIC-PID adaptive learning rate responses for (a) the amygdala $\tilde{\alpha}_{11}$, (b) the orbitofrontal cortex $\tilde{\beta}_{11}$, and (c) the thalamus $\tilde{\varepsilon}_{11}$ in example 2 (Gantry crane system).

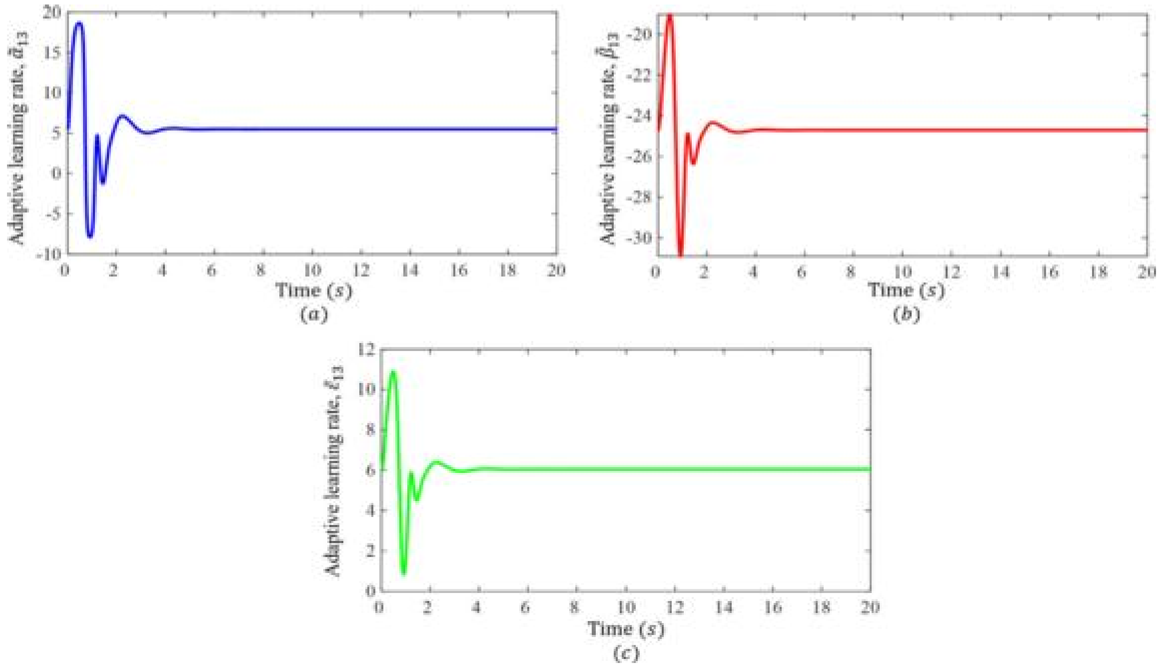

Fig. 37. The SbLR-BELBIC-PID adaptive learning rate responses for (a) the amygdala $\tilde{\alpha}_{13}$, (b) the orbitofrontal cortex $\tilde{\beta}_{13}$, and (c) the thalamus $\tilde{\varepsilon}_{13}$ in example 2 (Gantry crane system).

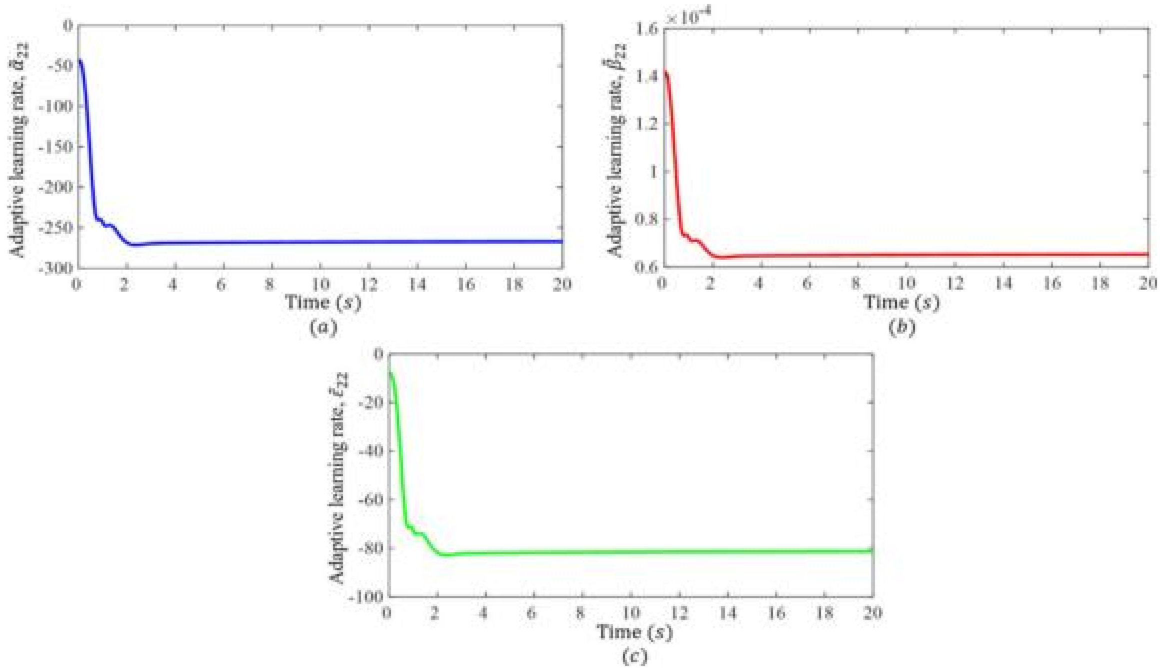

Fig. 38. The SbLR-BELBIC-PID adaptive learning rate responses for (a) the amygdala $\tilde{\alpha}_{22}$, (b) the orbitofrontal cortex $\tilde{\beta}_{22}$, and (c) the thalamus $\tilde{\varepsilon}_{22}$ in example 2 (Gantry crane system).

Table 11
Numerical results under measurement noise for Example 2 (Gantry crane system).

Performance Index	BELBIC-PID [58]	SbLR-BELBIC-PID
Fitness function J	230.8526	**209.5082**
ISE $\sum_{j=1}^{3} \bar{e}_j$	0.7983	**0.7159**
ISI $\sum_{i=1}^{2} \bar{u}_i$	32.6887	**28.8476**

Table 12
Trajectory tracking performance indices under measurement noise for Example 2 (Gantry crane system).

Response	Performance parameters	BELBIC-PID [58]	SbLR-BELBIC-PID
Trolley displacement, $y_1(t)$	ITAE	4.3063	**1.3223**
	ITSE	0.2312	**0.1399**
	IAE	1.0256	**0.7356**
	ISE	0.4491	**0.4078**
Rope length, $y_2(t)$	ITAE	1.1993	**0.7100**
	ITSE	0.0578	**0.0387**
	IAE	0.5605	**0.4320**
	ISE	0.1925	**0.1874**
Payload sway angle, $y_3(t)$	ITAE	1.0333	**0.6953**
	ITSE	0.1288	**0.0831**
	IAE	0.5303	**0.4211**
	ISE	0.1567	**0.1207**

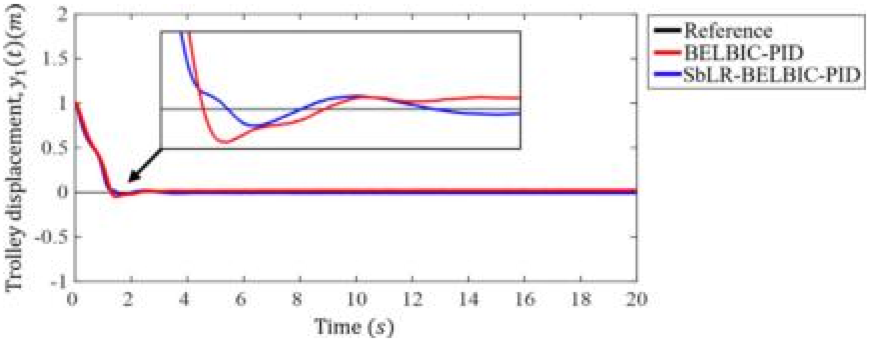

Fig. 39. The gantry crane trolley displacement, $y_1(t)$ responses under measurement noise.

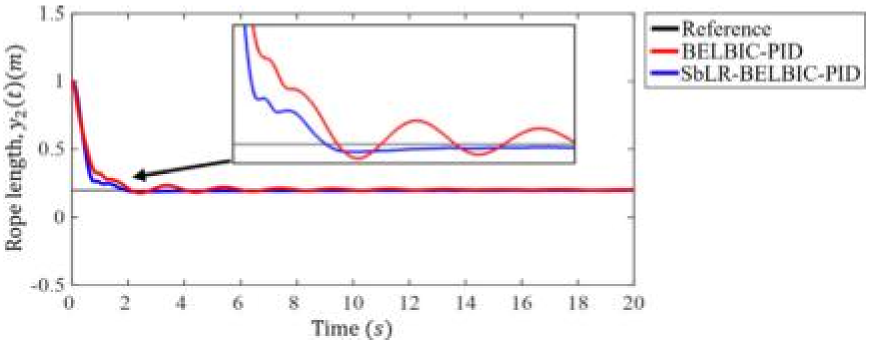

Fig. 40. The gantry crane rope length, $y_2(t)$ responses under measurement noise.

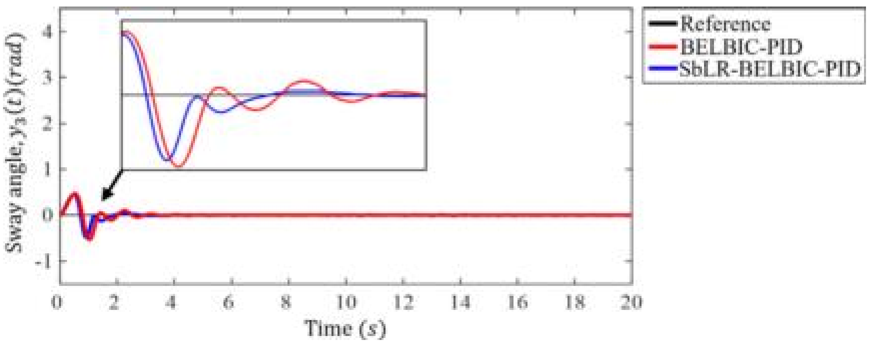

Fig. 41. The gantry crane payload sway angle, $y_3(t)$ responses under measurement noise.

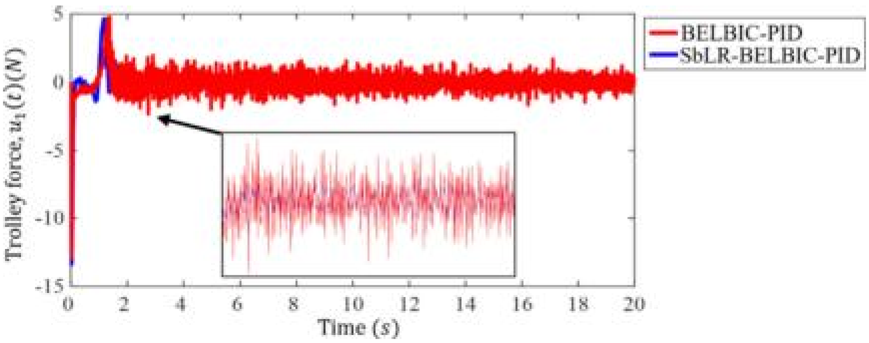

Fig. 42. The gantry crane trolley force, $u_1(t)$ responses under measurement noise.

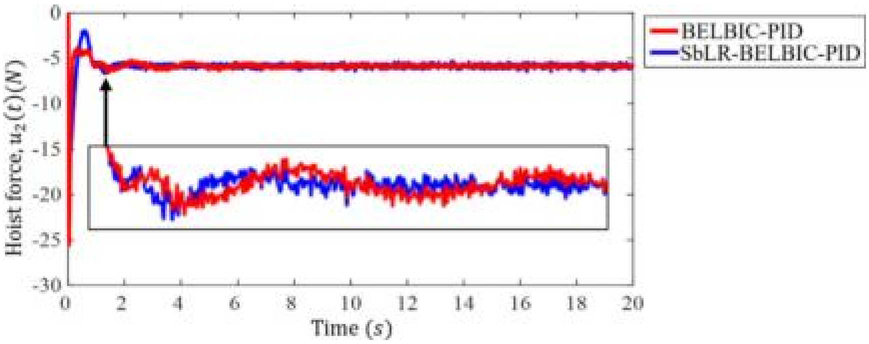

Fig. 43. The gantry crane hoist force, $u_2(t)$ responses under measurement noise.

6. Conclusion

This study presented the SbLR-BELBIC-PID controller, which integrates a sigmoid-based adaptive learning rate to overcome the restrictions of fixed-rate emotional learning in standard BELBIC-PID controllers, while addressing the challenges of controlling nonlinear multi-input multi-output (MIMO) systems with strongly coupled dynamics. By dynamically adjusting the learning rate according to the magnitude of the error signal, the proposed controller demonstrated enhanced adaptability and greater flexibility in its control outputs.

Simulation results on two benchmark MIMO systems, TRMS and the gantry crane, validated the superior performance of the SbLR-BELBIC-PID, demonstrating notable improvements in control accuracy, with a 5.24 % enhancement for TRMS and a 7.82 % improvement for the gantry crane relative to the standard BELBIC-PID. In addition, the controller exhibited improved time response characteristics, including reduced settling time, rise time, and overshoot, for TRMS horizontal and vertical trajectory tracking, as well as for gantry crane displacement, payload rope length, and sway angle control, consistently outperforming conventional PID, NEPID, and standard BELBIC-PID controllers.

These findings highlight the effectiveness of the proposed controller in optimizing trajectory tracking performance, as evidenced by reduced integral square error and smoother control inputs. By dynamically adjusting the learning rate, the controller mitigates undesirable behaviors associated with fixed-rate emotional learning, thereby further improving control accuracy. This effect is particularly evident during the initial simulation phase, where large error signals prompt rapid adaptation of the learning rate, allowing accurate trajectory tracking before stabilization. The results also support preliminary partial-SbLR studies, indicating that simultaneous adaptation of all BELBIC components further enhances control accuracy.

Moreover, robustness evaluations under measurement noise, based on IAE, ISE, ITAE, and ITSE indices, consistently showed lower values compared to the standard BELBIC-PID, confirming superior trajectory-tracking performance and improved responsiveness. Although this study focused on simulation validation, it lays a solid foundation for future experimental implementation. Further research could explore advanced reward-punishment formulations and memory-based learning to enhance adaptability and overall control performance. Additionally, hybridizing BELBIC-PID with other brain-inspired controllers, such as the cerebellar model articulation controller (CMAC), could leverage complementary brain-region functionalities to further improve control performance.

Overall, the SbLR-BELBIC-PID framework significantly advances intelligent control for complex MIMO applications, promoting the integration of bio-inspired emotional learning-based controllers into real-world engineering practice.

Declaration of competing interest

The authors declare that they have no known competing financial interests or personal relationships that could have appeared to influence the work reported in this paper.

CRediT authorship contribution statement

Shahrizal Saat: Writing – review & editing, Writing – original draft, Visualization, Methodology, Investigation, Formal analysis, Data curation, Conceptualization. **Mohd Ashraf Ahmad:** Writing – review & editing, Writing – original draft, Visualization, Validation, Supervision, Project administration, Formal analysis, Data curation, Conceptualization. **Mohd Riduwan Ghazali:** Validation, Resources, Project administration, Methodology, Formal analysis, Data curation, Conceptualization. **Mohd Helmi Suid:** Resources, Project administration, Funding acquisition, Data curation, Conceptualization.

Acknowledgment

We thank the Ministry of Higher Education for funding this research through the Fundamental Research Grant Scheme (FRGS) No. FRGS/1/2024/TK07/UMP/03/1 (University reference RDU240101). We also sincerely thank Universiti Teknikal Malaysia Melaka and Universiti Malaysia Pahang Al-Sultan Abdullah for their invaluable support, which was instrumental in the successful completion of this study.

Appendix A. Symbols and parameters

Table A1

List of symbols and parameters applied in the proposed SbLR-BELBIC-PID controlled MIMO systems.

Symbol	Description
p	Number of system inputs
q	Number of system outputs
y	System output responses
y'	System output responses under noise measurement
u	System control inputs responses
r	Reference signal
e	Error signal
e_{noise}	Noise measurement signal
k	Current iteration
k_{max}	Maximum number of iterations
λ	Coefficient factor for MSEDA
E	Probability coefficient for SEDA
x_i	Design parameters for i-th element
x_{min}	Lower bound for design parameters
x_{max}	Upper bound for design parameters
w_{ij}	Weight coefficient for (i, j)-th element
$J(\boldsymbol{\psi})$	Fitness function
$\boldsymbol{\psi}_{opt}$	Vector of optimal control parameters
$K_{P\ ij}^{SI}$	Proportional gain of the sensory input for (i, j)-th element
$K_{I\ ij}^{SI}$	Integral gain of the sensory input for (i, j)-th element
$K_{D\ ij}^{SI}$	Derivative gain of the sensory input for (i, j)-th element
N_{ij}^{SI}	Filter coefficient of the sensory input for (i, j)-th element
$K_{P\ ij}^{RW}$	Proportional gain of the reward signal for (i, j)-th element
$K_{I\ ij}^{RW}$	Integral gain of the reward signal for (i, j)-th element
$K_{D\ ij}^{RW}$	Derivative gain of the reward signal for (i, j)-th element
N_{ij}^{RW}	Filter coefficient of the reward signal for (i, j)-th element
ε	Fixed learning rate of thalamus (BELBIC PID)
α	Fixed learning rate of amygdala (BELBIC PID)
β	Fixed learning rate of orbitofrontal cortex (BELBIC-PID)
$\tilde{\varepsilon}_{ij}$	Adaptive learning rate of thalamus (SbLR-BELBIC PID) for (i, j)-th element
$\tilde{\alpha}_{ij}$	Adaptive learning rate of amygdala (SbLR-BELBIC-PID) for (i, j)-th element
$\tilde{\beta}_{ij}$	Adaptive learning rate of orbitofrontal cortex (SbLR-BELBIC-PID)for (i, j)-th element
$\varepsilon_{\max\ ij}$	Upper bound of thalamus adaptive learning rate for (i, j)-th element
$\varepsilon_{\min\ ij}$	Lower bound of thalamus adaptive learning rate for (i, j)-th element
$\alpha_{\max\ ij}$	Upper bound of amygdala adaptive learning rate for (i, j)-th element
$\alpha_{\min\ ij}$	Lower bound of amygdala adaptive learning rate for (i, j)-th element
$\beta_{\max\ ij}$	Upper bound of orbitofrontal cortex adaptive learning rate for (i, j)-th element
$\beta_{\min\ ij}$	Lower bound of orbitofrontal cortex adaptive learning rate for (i, j)-th element
σ_{ij}	Coefficient for $\tilde{\varepsilon}_{ij}$ sharpness for (i, j)-th element
γ_{ij}	Coefficient for $\tilde{\alpha}_{ij}$ sharpness for (i, j)-th element
ζ_{ij}	Coefficient for $\tilde{\beta}_{ij}$ sharpness for (i, j)-th element
$\Delta\varepsilon_{ij}$	Range of thalamus adaptive learning rate for (i, j)-th element
$\Delta\alpha_{ij}$	Range of amygdala adaptive learning rate for (i, j)-th element
$\Delta\beta_{ij}$	Range of orbitofrontal cortex adaptive learning rate for (i, j)-th element
m_{ij}	Controller function for sensory input for (i, j)-th element
n_{ij}	Controller function for reward signal for (i, j)-th element
a_{ij}	Controller function for amygdala for (i, j)-th element
o_{ij}	Controller function for orbitofrontal cortex for (i, j)-th element
l_{ij}	Controller function for thalamus for (i, j)-th element

References

[1] V.K. Pandey, I. Kar, C. Mahanta, Controller design for a class of nonlinear MIMO coupled system using multiple models and second level adaptation, ISA Trans. 69 (2017) 256–272, doi:10.1016/j.isatra.2017.05.005.

[2] A.F. Amer, E.A. Sallam, W.M. Elawady, Adaptive fuzzy sliding mode control using supervisory fuzzy control for 3 DOF planar robot manipulators, Appl. Soft. Comput. 11 (2011) 4943–4953, doi:10.1016/j.asoc.2011.06.005.

[3] M. Abdillah, E.M. Mellouli, T. Haidi, A new intelligent controller based on integral sliding mode control and extended state observer for nonlinear MIMO drone quadrotor, Int. J. Intell. Netw. 5 (2024) 49–62, doi:10.1016/j.ijin.2024.01.005.

[4] X. Yang, J. Cui, D. Lao, D. Li, J. Chen, Input shaping enhanced active disturbance rejection control for a win rotor multi-input multi-output system (TRMS), ISA Trans. 62 (2016) 287–298, doi:10.1016/j.isatra.2016.02.001.

[5] J.W. Wang, H.N. Wu, H.X. Li, Static output feedback control design for linear MIMO systems with actuator dynamics governed by diffusion PDEs, Int. J. Control 87 (2014) 90–100, doi:10.1080/00207179.2013.822991.
[6] R. Guardeño, M.J. López, V.M. Sánchez, MIMO PID controller tuning method for quadrotor based on LQR/LQG theory, Robotics 8 (2019) 36, doi:10.3390/ROBOTICS8020036.
[7] N. Abbas, X. Liu, J. Iqbal, A flexible mixed-optimization with H∞ control for coupled twin rotor MIMO system based on the method of inequality (MOI)- an experimental study, PLoS One 19 (2024), doi:10.1371/journal.pone.0300305.
[8] P. Yan, D. Liu, D. Wang, H. Ma, Data-driven controller design for general MIMO nonlinear systems via virtual reference feedback tuning and neural networks, Neurocomputing 171 (2016) 815–825, doi:10.1016/j.neucom.2015.07.017.
[9] W. Tang, P. Daoutidis, Data-driven control: overview and perspectives, in: Proceedings of the 2022 American Control Conference (ACC), Atlanta, GA, USA, 2022, pp. 1048–1064, doi:10.23919/ACC53348.2022.9867266.
[10] Z. Hou, X. Bu, Model free adaptive control with data dropouts, Expert Syst. Appl. 38 (2011) 10709–10717, doi:10.1016/j.eswa.2011.01.158.
[11] Z.S. Hou, Z. Wang, From model-based control to data-driven control: survey, classification and perspective, Inf. Sci. (N.Y.) 235 (2013) 3–35, doi:10.1016/j.ins.2012.07.014.
[12] M.A. Ahmad, S.I. Azuma, T. Sugie, Performance analysis of model-free PID tuning of MIMO systems based on simultaneous perturbation stochastic approximation, Expert Syst. Appl. 41 (2014) 6361–6370, doi:10.1016/j.eswa.2014.03.055.
[13] N.F. Nanyan, M.A. Ahmad, B. Hekimoğlu, Optimal PID controller for the DC-DC buck converter using the improved sine cosine algorithm, Results Control Optim. 14 (2024), doi:10.1016/j.rico.2023.100352.
[14] T. Yamamoto, K. Takao, T. Yamada, Design of a data-driven PID controller, IEEE Trans. Control. Syst. Technol. 17 (2009) 29–39, doi:10.1109/TCST.2008.921808.
[15] Z. Hu, W. Guo, K. Zhou, L. Wang, F. Wang, J. Yuan, Optimization of PID control parameters for marine dual-fuel engine using improved particle swarm algorithm, Sci. Rep. 14 (2024), doi:10.1038/s41598-024-63253-y.
[16] I. Anshory, J. Jamaaluddin, A. Wisaksono, I. Sulistiyowati, Hindarto, B.S. Rintyarna, A. Fudholi, Y.A. Rahman, K. Sopian, Optimization DC-DC boost converter of BLDC motor drive by solar panel using PID and firefly algorithm, Results Eng. 21 (2024), doi:10.1016/j.rineng.2023.101727.
[17] K. Jagatheesan, D. Boopathi, S. Samanta, B. Anand, N. Dey, Grey wolf optimization algorithm-based PID controller for frequency stabilization of interconnected power generating system, Soft. Comput. 28 (2024) 5057–5070, doi:10.1007/s00500-023-09213-6.
[18] M. Akhtaruzzaman, A.A. Shafie, M.R. Khan, M.M. Rahman, Robot assisted knee joint RoM exercise: a PID parallel compensator architecture through impedance estimation, Cogn. Robot. 4 (2024) 42–61, doi:10.1016/j.cogr.2023.11.003.
[19] K.J. Astrom, T. Hagglund, The future of PID control, Control Eng. Pr. 9 (2001) 1163–1175, doi:10.1016/S0967-0661(01)00062-4.
[20] I. Lopez-Sanchez, J. Moreno-Valenzuela, PID control of quadrotor UAVs: a survey, Annu. Rev. Control 56 (2023), doi:10.1016/j.arcontrol.2023.100900.
[21] J.G. Juang, R.W. Lin, W.K. Liu, Comparison of classical control and intelligent control for a MIMO system, Appl. Math. Comput. 205 (2008) 778–791, doi:10.1016/j.amc.2008.05.061.
[22] A. Prabhakaran, T. Ponnusamy, Thenmozhi, G. Janarthanan, Optimized fractional order PID controller with sensorless speed estimation for torque control in induction motor, Expert Syst. Appl. 249 (2024), doi:10.1016/j.eswa.2024.123574.
[23] C. Ben Djaballah, W. Nouibat, R. Ayad, Optimization of fractional-order PI-PID controllers for MIMO systems using artificial bee colony algorithm, Soft. Comput. 28 (2024) 10281–10299, doi:10.1007/s00500-024-09776-y.
[24] M.I.P. Azahar, A. Irawan, R.M.T. Raja Ismail, Adjustable convergence rate prescribed performance with fractional-order PID controller for Servo pneumatic actuated robot positioning, Cogn. Robot. 3 (2023) 93–106, doi:10.1016/j.cogr.2023.04.004.
[25] M.I. Abdo, E.A. Elsheikh, Optimization of a fractional-order interval type-2 fuzzy PID controller based on BBO for real-time applications, Frankl. Open 8 (2024) 100121, doi:10.1016/j.fraope.2024.100121.
[26] C. Ma, B. Huang, M.K. Basher, M.A. Rob, Y. Jiang, Fuzzy PID control design of mining electric locomotive based on permanent magnet synchronous motor, Electron (Basel) 13 (2024) 1855, doi:10.3390/electronics13101855.
[27] S.A. Hosseini, A.S. Shirani, M. Lotfi, M.B. Menhaj, Design and application of supervisory control based on neural network PID controllers for pressurizer system, Prog. Nucl. Energy 130 (2020) 103570, doi:10.1016/j.pnucene.2020.103570.
[28] S. Slama, A. Errachdi, M. Benrejeb, Neural adaptive PID and neural indirect adaptive control switch controller for nonlinear MIMO systems, Math. Probl. Eng. (2019) 7340392, doi:10.1155/2019/7340392.
[29] Q. Cheng, Y. Cheng, R. Guo, Y. Zheng, The forward NN-PID controllers based on chaos PSO-BP hybrid optimization algorithms for decoupling control system of ball mill, in: Proceedings of the 2009 International Conference on Artificial Intelligence and Computational Intelligence, Shanghai, China, 2009, pp. 189–193, doi:10.1109/AICI.2009.66.
[30] T.A. Nguyen, Research on the sliding mode – PID control algorithm tuned by fuzzy method for vehicle active suspension, Forces Mech. 11 (2023) 100206, doi:10.1016/j.finmec.2023.100206.
[31] C. Yang, F. Yao, M. Zhang, Z. Zhang, Z. Wu, P. Dan, Adaptive sliding mode PID control for underwater manipulator based on legendre polynomial function approximation and its experimental evaluation, Appl. Sci. 10 (2020) 1728, doi:10.3390/app10051728.
[32] L. Cheng, Z. Wang, F. Jiang, J. Li, Adaptive neural network control of nonlinear systems with unknown dynamics, Adv. Space Res. 67 (2021) 1114–1123, doi:10.1016/j.asr.2020.10.052.
[33] Z. Li, S. Li, Time-optimal constrained kinematic control of robotic manipulators by recurrent neural network, Expert Syst. Appl. 257 (2024), doi:10.1016/j.eswa.2024.124994.
[34] J. Wang, X. Liao, Z. Yi, B. Liu, L. Ren, Y. Ding, A novel intelligent controller based on modulation of neuroendocrine system, in: Advances in Neural Networks, Berlin, Heidelberg, 2005, pp. 119–124, doi:10.1007/11427469_18.
[35] Y. Ding, N. Xu, L. Ren, K. Hao, Data-driven neuroendocrine ultrashort feedback-based cooperative control system, IEEE Trans. Control. Syst. Technol. 23 (2015) 1205–1212, doi:10.1109/TCST.2014.2359386.
[36] M.R. Ghazali, M.A. Ahmad, R.M.T.R. Ismail, A multiple-node hormone regulation of neuroendocrine-PID (MnHR-NEPID) control for nonlinear MIMO systems, IETE J. Res. 68 (2020) 4476–4491, doi:10.1080/03772063.2020.1795939.
[37] M.R. Ghazali, M.A. Ahmad, R.M.T. Raja Ismail, M.O. Tokhi, An improved neuroendocrine–proportional–integral–derivative controller with sigmoid-based secretion rate for nonlinear multi-input–multi-output crane systems, J. Low. Freq. Vib. Act. Control. 39 (2020) 1172–1186, doi:10.1177/1461348419867524.
[38] K. Takahashi, T. Yamada, Application of an immune feedback mechanism to control system, JSME Int. J. 41 (1998) 184–191, doi:10.1299/jsmec.41.184.
[39] Y. Ding, T. Zhang, L. Ren, Y. Jin, K. Hao, L. Chen, Immune-inspired self-adaptive collaborative control allocation for multi-level stretching processes, Inf. Sci. (N.Y.) 342 (2016) 81–95, doi:10.1016/j.ins.2015.12.029.
[40] C. Lucas, D. Shahmirzadi, N. Sheikholeslami, Introducing BELBIC: brain emotional learning based intelligent controller, Intell. Autom. Soft. Comput. 10 (2004) 11–21, doi:10.1080/10798587.2004.10642862.
[41] E. Lotfi, A.A. Rezaee, Generalized BELBIC, Neural. Comput. Appl. 31 (2019) 4367–4383, doi:10.1007/s00521-018-3352-1.
[42] C. Balkenius, J. Morén, Emotional learning: a computational model of the amygdala, Cybern. Syst. 32 (2001) 611–636, doi:10.1080/019697201750361283.
[43] E. Lotfi, S. Setayeshi, S. Taimory, A neural basis computational model of emotional brain for online visual object recognition, Appl. Artif. Intell. 28 (2014) 814–834, doi:10.1080/08839514.2014.952924.
[44] S.H. Fakhrmoosavy, S. Setayeshi, A. Sharifi, An intelligent method for generating artificial earthquake records based on hybrid PSO–parallel brain emotional learning inspired model, Eng. Comput. 34 (2018) 449–463, doi:10.1007/s00366-017-0551-9.
[45] C. Lucas, R.M. Milasi, B.N. Araabi, Intelligent modeling and control of washing machine using locally linear neuro-fuzzy (LLNF) modeling and modified brain emotional learning based intelligent controller (BELBIC), Asian J. Control. 8 (2006) 393–400, doi:10.1111/j.1934-6093.2006.tb00290.x.
[46] H. Rouhani, M. Jalili, B.N. Araabi, W. Eppler, C. Lucas, Brain emotional learning based intelligent controller applied to neurofuzzy model of micro-heat exchanger, Expert Syst. Appl. 32 (2007) 911–918, doi:10.1016/j.eswa.2006.01.047.

[47] A. Reza Mehrabian, C. Lucas, Intelligent adaptive control of non-linear systems based on emotional learning approach, Int. J. Artif. Intell. Tools 16 (2007) 69–85, doi:10.1142/S0218213007003205.
[48] A. Vargas-Clara, S. Redkar, Unmanned ground vehicle navigation using brain emotional learning based intelligent controller (BELBIC), Smart Sci. 3 (2015) 10–15, doi:10.1080/23080477.2015.11665631.
[49] E. Daryabeigi, H. Abootorabi Zarchi, G.R. Arab Markadeh, J. Soltani, F. Blaabjerg, Online MTPA control approach for synchronous reluctance motor drives based on emotional controller, IEEE Trans. Power. Electron. 30 (2015) 2157–2166, doi:10.1109/TPEL.2014.2323180.
[50] M.D. Qutubuddin, B.S. Raju, N. Yadaiah, Performance analysis of brain emotional controller for rotary inverted pendulum system, in: Proceedings of the 2017 14th IEEE India Council International Conference (INDICON), Roorkee, India, 2017, pp. 1–6, doi:10.1109/INDICON.2017.8488015.
[51] P. Sharma, V. Kumar, Design and analysis of novel bio inspired BELBIC and PSOBELBIC controlled semi active suspension, Int. J. Veh. Perform. 6 (2020) 399–424, doi:10.1504/IJVP.2020.111407.
[52] C. Kim, J. Suh, J.H. Han, Development of a hybrid path planning algorithm and a bio-inspired control for an omni-wheel mobile robot, Sensors 20 (2020) 1–22, doi:10.3390/s20154258.
[53] M.S.O. Yeganeh, A. Oshnoei, N. Mijatovic, T. Dragicevic, F. Blaabjerg, Intelligent secondary control of islanded AC microgrids: a brain emotional learning-based approach, IEEE Trans. Ind. Electron. 70 (2022) 6711–6723, doi:10.1109/TIE.2022.3203677.
[54] S. Saat, M.R. Ghazali, M.A. Ahmad, N.M.Z.A. Mustapha, M.Z.M. Tumari, An implementation of brain emotional learning-based intelligent controller for AVR system, in: Proceedings of the 2023 IEEE International Conference on Automatic Control and Intelligent Systems (I2CACIS), Shah Alam, Malaysia, 2023, pp. 60–64, doi:10.1109/I2CACIS57635.2023.10193647.
[55] A.A. Zamani, S. Etedali, A new framework of multi-objective BELBIC for seismic control of smart base-isolated structures equipped with MR dampers, Eng. Comput. 38 (2022) 3759–3772, doi:10.1007/s00366-021-01414-7.
[56] M.U. Saeed, Z. Sun, S. Elias, Semi-active vibration control of building structure by self tuned brain emotional learning based intelligent controller, J. Build. Eng. 46 (2022) 103664–103688, doi:10.1016/j.jobe.2021.103664.
[57] M.B. César, J.P. Coelho, J. Gonçalves, Semi-active vibration control of a non-collocated civil structure using evolutionary-based BELBIC, Actuators 8 (2019) 1–19, doi:10.3390/act8020043.
[58] S. Saat, M.A. Ahmad, M.R. Ghazali, Data-driven brain emotional learning-based intelligent controller-PID control of MIMO systems based on a modified safe experimentation dynamics algorithm, Int. J. Cogn. Comput. Eng. 6 (2025) 74–99, doi:10.1016/j.ijcce.2024.11.005.
[59] H. Zhao, H. Wang, B. Niu, X. Zhao, N. Xu, Adaptive fuzzy decentralized optimal control for interconnected nonlinear systems with unmodeled dynamics via mixed data and event driven method, Fuzzy. Sets. Syst. 474 (2024) 108735, doi:10.1016/j.fss.2023.108735.
[60] I.A. Zamfirache, R.E. Precup, R.-C. Roman, E.M. Petriu, Neural network-based control using actor-critic reinforcement learning and grey wolf optimizer with experimental servo system validation, Expert Syst. Appl. 225 (2023) 120112, doi:10.1016/j.eswa.2023.120112.
[61] X. Deng, C. Zhang, Y. Ge, Adaptive neural network dynamic surface control of uncertain strict-feedback nonlinear systems with unknown control direction and unknown actuator fault, J. Frankl. Inst. 359 (2022) 4054–4073, doi:10.1016/j.jfranklin.2022.04.010.
[62] M.Z. Mohd Tumari, M.A. Ahmad, M.H. Suid, M.R. Ghazali, M.O. Tokhi, An improved marine predators algorithm tuned data-driven multiple-node hormone regulation neuroendocrine-PID controller for multi-input–multi-output gantry crane system, J. Low. Freq. Noise Vib. Act. Control. 42 (2023) 1666–1698, doi:10.1177/14613484231183938.
[63] A. Ates, B.B. Alagoz, H. Alisoy, Sigmoid-based PID controller implementation for rotor control, in: Proceedings of the 2015 European Control Conference (ECC), Linz, Austria, 2015, pp. 458–463, doi:10.1109/ECC.2015.7330586.
[64] M. Kharrat, M. Krichen, H. Alhazmi, P. Mercorelli, Neural network-based adaptive fault-tolerant control for strict-feedback nonlinear systems with input dead zone and saturation, J. Frankl. Inst. 362 (2025) 107471, doi:10.1016/j.jfranklin.2024.107471.
[65] L. Liu, Y.J. Liu, A. Chen, Integral barrier Lyapunov function-based adaptive control for switched nonlinear systems, Sci. China Inf. Sci. 63 (2020) 132203, doi:10.1007/s11432-019-2714-7.
[66] S. Khorashadizadeh, S.M.H. Zadeh, M.R. Koohestani, Robust model-free control of a class of uncertain nonlinear systems using BELBIC: stability analysis and experimental validation, J. Braz. Soc. Mech. Sci. Eng. 41 (2019) 311, doi:10.1007/s40430-019-1824-6.
[67] J.R. Marden, H.P. Young, G. Arslan, J.S. Shamma, Payoff-based dynamics for multiplayer weakly acyclic games, SIAM J. Control. Optim. 48 (2009) 373–396, doi:10.1137/070680199.
[68] N.S.A. Shukor, M.A. Ahmad, M.Z.M. Tumari, Data-driven PID tuning based on safe experimentation dynamics for control of liquid slosh, in: Proceedings of the 2017 IEEE 8th Control and System Graduate Research Colloquium (ICSGRC), Shah Alam, Malaysia, 2017, pp. 62–66, doi:10.1109/ICSGRC.2017.8070569.
[69] M.R. Ghazali, M.A. Ahmad, M.F.M. Jusof, R.M.T.R. Ismail, A data-driven neuroendocrine PID controller for underactuated systems based on safe experimentation dynamics, in: Proceedings of the 2018 IEEE 14th International Colloquium on Signal Processing and Its Applications (CSPA), Penang, Malaysia, 2018, pp. 61–66, doi:10.1109/CSPA.2018.8368686.
[70] Twin Rotor System Advanced Teaching Manual 1 (33-007-4M5), Feedback Instruments Ltd, M.I.M.O, Crowborough, 1998.
[71] H. Park, D. Chwa, K.-S. Hong, A feedback linearization control of container cranes: varying rope length, Int. J. Control. Autom. Syst. 5 (2007) 379–387 https://api.semanticscholar.org/CorpusID:55820225.
[72] M.S. Park, D. Chwa, M. Eom, Adaptive sliding-mode antisway control of uncertain overhead cranes with high-speed hoisting motion, IEEE Trans. Fuzzy. Syst. 22 (2014) 1262–1271, doi:10.1109/TFUZZ.2013.2290139.